THESIS FOR THE DEGREE OF LICENTIATE OF ENGINEERING

Rapid Aerodynamic Method for Interacting Sails

KAROLINA MALMEK

Department of Mechanics and Maritime Sciences
CHALMERS UNIVERSITY OF TECHNOLOGY
Gothenburg, Sweden 2023

Rapid Aerodynamic Method for Interacting Sails

KAROLINA MALMEK

Report No 2023:06

Chalmers University of Technology
Department of Mechanics and Maritime Sciences
SE-412 96, Gothenburg
Sweden
Telephone: +46 (0)31-772 1000
www.chalmers.se

Typeset by the author using LaTeX
Printed by Chalmers Reproservice
Gothenburg, Sweden, 2023

Rapid Aerodynamic Method for Interacting Sails

KAROLINA MALMEK
Chalmers University of Technology
Department of Mechanics and Maritime Sciences

Abstract

Rapid performance prediction tools are required for the evaluation, optimization, and comparison of different wind propulsion systems (WPSs). These tools should capture viscous aerodynamic flow effects in 3D, especially the maximum propulsion force, stall angles and interaction effects between the lift-generating units. This thesis presents such a rapid aerodynamic calculation method that combines viscous pre-tabulated data with an inviscid lifting line/potential flow model to account for 3D sail–sail interaction effects.

The proposed method was evaluated in two validation studies; in the first study, validation data was obtained via CFD simulations and in the second via wind tunnel tests. The WPS test case consisted of multiple wingsails.

The results showed that the interaction model improved the prediction considerably compared to when interaction was not accounted for. The interaction affected the generated total driving force and especially the moment, which was well predicted by the method. The angle sweep studies indicated that the method could predict the maximum driving force and the stall angles of the sails with acceptable accuracy. Compared to 3D CFD simulations or wind tunnel testing the computational cost of the method was negligible.

This thesis concludes that the proposed rapid method is a suitable complement to more costly high-fidelity tools. Its ability to predict how the forces and moments change due to sail–sail interaction effects is important because it impacts the overall performance of the ship. Future work will include further validation studies for different WPS configurations, evaluation of possible method improvements and investigations on how to implement of the method in the ship design process.

Keywords: wind-assisted propulsion, wind propulsion system, sail–sail interaction, lifting line method, wingsail

Preface

The research project presented in this licentiate thesis has been performed at the Division of Marine Technology, Department of Mechanics and Marine Sciences at Chalmers University of Technology and at RISE - Research Institutes of Sweden (former SSPA Sweden AB, www.sspa.se). The research was funded by the Swedish Transport Agency (grant TRV 2018/96451) through the *wPCC - wind Powered Car Carrier* project and the Swedish Energy Agency (grant 2022/P2021-00275) through the *Multiwind - Multi-fidelity methods for design and evaluation of wind-powered vessels* project.

My life circles around sailing, and I am so grateful for having been given the opportunity to explore some of the physics behind it. Throughout this project my main supervisor Professor Emeritus Lars Larsson has been an unfaltering source of knowledge, inspiring discussions and support. It has been deeply encouraging to see his strong devotion to and continued curiosity on the subject, soon 50 years after his own dissertation on sailing and fluid dynamics.

I am thankful for the support I have received from my supervisors at the Division of Marine Technology, my examiner Professor Jonas W. Ringsberg and Professor Rickard Bensow. At RISE/SSPA Dr. Sofia Werner, lead researcher in hydrodynamics and wind powered ships, took a major part in initiating the project and also acted as supervisor together with Dr. Christian Finnsgård, head of Maritime Research. All of you have been more than helpful in guiding me and providing the different tools I needed to finish this work.

I also want to thank the larger group of PhD students and researchers I have been collaborating with at RISE/SSPA, Chalmers University of Technology and KTH Royal Institute of Technology, all working in different areas within wind propulsion. Exploring this (re-)emerging field together with you has given me invaluable input and a good portion of fun along the way.

Karolina Malmek
Göteborg, March 2023

Contents

List of Publications

This monograph thesis is partly based on material previously published in the following publications:

[**Paper I**] **K. Malmek**, L. Larsson, S. Werner, J. W. Ringsberg, R. Bensow and C. Finnsgård. Rapid aerodynamic method for predicting the performance of interacting sails on wind powered ships. Submitted to *Ocean Engineering*, under review.
Contribution: conceptualization, methodology, software, validation, investigation, writing–original draft preparation, visualization

[**Paper II**] **K. Malmek**, U. Dhomé, L. Larsson, S. Werner, J. W. Ringsberg and C. Finnsgård. Comparison of two rapid numerical methods for predicting the performance of multiple rigid wind-sails. *5th International Conference on Innovation in High Performance Sailing Yachts and Sail-Assisted Ship Propulsion (June 2020), Gothenburg, Sweden.*
Contribution: conceptualization, methodology, software, validation, investigation, writing–original draft preparation, visualization

Other relevant publications co-authored by Karolina Malmek:

[**Paper III**] L. Marimon Giovannetti, U. Dhomé, **K. Malmek**, A. Persson and C. Wielgosz. Multi-wing sails interaction effects. *The 24th Chesapeake Sailing Yacht Symposium (June 2022), Annapolis, Maryland.*
Contribution: methodology, investigation, writing–review and editing

Nomenclature

α	angle of attack
β_{AW}	apparent wind angle
Γ	circulation strength
∞	indicating undisturbed flow characteristic
$\mathbf{r}$	distance vector
$\mathbf{V}$	wind vector
ρ	density of air
AR	aspect ratio
b	wingsail span
c	chord length
C_D	3D drag force coefficient
c_d	2D drag force coefficient
C_D^{2D}	integrated 3D drag force coefficient
C_L	3D lift force coefficient
c_l	2D lift force coefficient
C_L^{2D}	integrated 3D lift force coefficient
C_M	3D yaw moment coefficient
c_m	2D yaw moment coefficient
C_X	3D driving force coefficient
c_x	2D driving force coefficient
C_Y	3D side force coefficient
c_y	2D side force coefficient
C_{D_i}	3D induced drag force coefficient
C_{pi}	induced pressure coefficient
d	leading edge to leading edge distance between sails

$d\mathbf{l}$	vortex filament
f	fraction in the boundary layer correction
i	as lowercase letter, index for sail number
i	as subscript, indicating interaction-induced flow characteristic
j	index for strip number on the sail of interest
loc	local flow characteristic
m	index for strip number on surrounding sail
n_{sails}	number of sails
S	sail surface area
s	sheeting angle
Re	Reynolds number

List of Acronyms

2D two-dimensional.

3D three-dimensional.

CFD computational fluid dynamics.

ISILL interacting sectionally integrated lifting-lines.

LCE longitudinal center of effort.

LE leading edge.

LLM lifting-line model.

LLT lifting-line theory.

PIV particle image velocimetry.

RANS Reynolds-averaged Navier–Stokes.

SILL sectional integration with lifting-line.

TAT thin-airfoil theory.

TE trailing edge.

VLM vortex lattice method.

VPP velocity prediction program.

WPS wind propulsion system.

WTT wind tunnel tests.

Chapter 1

INTRODUCTION

1.1 Research Background

Global trade has depended on shipping for centuries, to the extent that shipping has become a synonym for freight transport in general. Today, the global fleet of ships still relies almost exclusively on non-renewable fossil fuels, and the pathway toward its decarbonization is not set. In fact, long-haul shipping is still largely considered a "hard-to-abate" sector, and is at risk of increasing its share of global emissions as other industry sectors transition to other energy sources. Electrification, fuel cells, nuclear power or new types of fuels (e.g., hydrogen, ammonia or methanol) could offer carbon-neutral energy on some trading routes, but each of these technologies faces several challenges that are yet to be resolved (DNV, 2021).

The reintroduction of wind propulsion for commercial ships, which directly utilizes the wind to drive vessels forward, offers a large potential to reduce emissions from global shipping (Chou et al., 2020). If used in combination with other propulsion systems, it can extend the sailing range and lower the energy consumption for new builds and by retrofitting existing ships. In a world with volatile energy prices and limited global availability of several energy carriers, the possibility of directly harvesting wind energy on-board decreases operational costs (Gerhardt et al., 2022), thereby reducing financial risks as well as emissions.

Several different wind propulsion system (WPS) concepts have been suggested, of which variations of soft sails, Flettner rotors, kites, wingsails and sails with active circulation control have been employed (see the recent review by Cairns et al., 2021). In the wind-assisted propulsion segment, Flettner rotors are already in use. The reported energy savings from current installations vary and are highly dependent on the ship's operation and wind conditions. Some speed trials and reports of fuel consumption suggest savings of approximately ca 4-8% (Werner et al., 2021; Cairns et al., 2021) for single rotors. By using multiple rotors or other WPSs on the same ship, the fuel-saving potential can be much higher (Tillig, 2020; Lu and Ringsberg, 2020). For vessels purposely designed for wind propulsion, current design concepts aim at fuel savings greater than 50%, while maintaining acceptable speed and punctuality. One such concept is the *Oceanbird*; see Figure 1.1.

A WPS's performance en route and the resulting potential fuel savings are important factors in continued WPS development. Yet, such calculations are challenging from a computational perspective, requiring reliable and computationally efficient aerodynamic performance prediction methods. Such methods should be able to predict loads generated by WPSs for a large number of varying wind conditions and WPS

Some of the material in this chapter is, with minor adaptions and additions, extracted from Paper I; see the List of Publications.

configurations. In addition, for several types of WPSs, the maximum driving force is obtained when operating near maximum lift. This means that the methods must be able to predict when the sails will stall. Without this capability, the sheeting angles cannot be optimized.

Modeling aerodynamics using the classical inviscid potential flow theory is an option with high computational efficiency. Methods based on Prandtl's lifting-line theory (LLT) have been widely used in the aeronautics industry for the past hundred years (see Katz and Plotkin, 2001, or Anderson, 2017). Today, the strength of LLT is its simplicity in relation to potential flow-based panel methods and viscous simulation tools, such as computational fluid dynamics (CFD). Several adaptions of the theory have been made. For example, Phillips and Snyder (2000) and Cheng and Wang (2018) extended the classical LLT to several lifting surfaces in their studies of tandem airplane wings, and they concluded that the LLT-based methods could predict the inviscid loads generated by high-aspect-ratio lifting surfaces at low angles of attack with an accuracy as good as that obtained with modern panel codes or CFD. Spall et al. (2013) used LLT to model the interaction between a jib and a main sail for pre-stall angles.

Along with other potential flow methods, the LLT-based methods have the downside of not including viscous effects, such as viscous drag and stall, and cannot be used to predict maximum lift. Therefore, CFD and wind tunnel testing have been the two main tools for simulating interacting sails. For example, Nakashima et al. (2011) used large eddy simulation CFD and Ouchi et al. (2011) used Reynolds-averaged Navier–Stokes (RANS) CFD to model interacting WPSs in 3D. 2D RANS CFD has been combined with different optimization algorithms to find optimal sheeting angles (Chapin et al., 2006; Lee et al., 2016) and to optimize the parametric design of suction wingsails with active circulation control (Cairns et al., 2021). This 2D CFD optimization approach, which relies on surrogate models and response surfaces, does not consider the 3D effects on the sail–sail interaction and sheeting optimization.

Figure 1.1: Concept design of the car carrier Oceanbird (2021).

Extending the 2D CFD optimization to full 3D CFD would come at a (too) high computational cost. The list of possible design variables is long; a large number of 3D simulations is needed to evaluate the effects of different types of WPSs, deck placements, aerodynamic profiles, heights and planforms. In order to get an accurate estimate of the system's performance, each design candidate should preferably be evaluated en route under varying weather conditions, resulting in a large number of simulations for different combinations of wind strengths and apparent wind angles.

Several WPS concepts have been tested in wind tunnel experiments, such as those of Ingham and Tersløv (1985), Fujiwara et al. (2005), Li et al. (2015) and Bordogna et al. (2018). Marimon Giovannetti et al. (2022) performed wind tunnel tests for the interacting wingsails of the Oceanbird. Wind tunnel testing remains an important tool for validating simulations and final concepts, but it generally comes at too high a cost to be used to evaluate multiple concepts at early design stages or for optimization. Additionally, some aerodynamic effects may not be accurately captured at model scale.

Therefore, there is a strong need for a method that is both computationally efficient and includes the effect of viscosity, particularly close to stall. Such a method was presented by Graf et al. (2014). They combined a 3D non-linear lifting-line model with viscous 2D data and applied it to a wingsail. Based on their study, Persson et al. (2019) developed another lifting-line algorithm method called *sectional integration with lifting-line (SILL)* that assumes an elliptical lift distribution along the span. 2D CFD data were used as input, and the method was compared with 3D RANS-CFD simulations. It was concluded that the SILL method had good potential to predict both generated forces and the point of stall for a single wingsail.

However, Persson et al. (2019) did not consider the interaction effects between several sails or rotors. Such effects may be considerable, as indicated, for instance, by the wind tunnel tests with interacting rigid wingsails that Bordogna et al. (2018) performed. Changes in sail loading due to such interaction were seen when the sail distances ranged from one to three times the chord lengths. The optimal sheeting angles also changed; in their study of the performance of multiple sails, Li et al. (2015) found that the thrust of the interacting sails increased by 42.3% when the sails were sheeted independently. Bordogna (2020) validated a mathematical method, applying a potential flow-based horseshoe vortex interaction model against wind tunnel tests with two wingsails respectively two Flettner rotors. This method also considered some viscous effects based on semi-empirical formulas. In the study, Bordogna concluded that the proposed method was able to predict some of the interaction effects but failed to predict the interaction effects for a majority of the tested apparent wind angles.

An aerodynamic method is needed that is rapid and considers both the viscosity and the interaction effects between sails or rotors. Such a method was first presented by Malmek et al. (2020) in a preliminary report. Another potential flow-based interaction method for Flettner rotors that considers the interaction in the 2D horizontal plane was later developed and tested by Tillig and Ringsberg (2020). However, this method cannot be applied to wingsails. In this thesis, a 3D method for interacting wingsails

that has the necessary capabilities is described. This is done by extending the SILL method developed for one wingsail to multiple sails. The new method is called *interacting sectionally integrated lifting-lines (ISILL)*.

1.2 Research Questions

The aim of the research presented in this thesis is to formulate an aerodynamic method for multiple interacting sails. The method should be suitable for application in time efficient velocity prediction programs (VPPs) that are used for predicting the performance of ships equipped with WPSs. Therefore, three key requirements on the method is that it has low computational cost, that it can be used for sheeting optimization to find the maximum driving force and that it can estimate the yaw moment generated by the sails.

To aid in this aim, two main research questions are addressed below.

RQ1: How can a rapid aerodynamic method that handles sail–sail interaction and viscous effects be formulated?

When addressing RQ1, previous rapid methods for single sail systems that consider viscous effects by combining viscous data with lifting-line theory are used as a basis. The SILL method, introduced in Section 1.1, is selected as a suitable candidate for further development. The main contribution in this thesis is therefore to formulate an efficient model for the sail–sail interaction effects and integrate it with the existing single sail method.

RQ1: How accurate is the proposed method in terms of predicting the driving force, the moments and the point of stall?

Having formulated a method, RQ1 addresses weather the method fulfills the set requirements or not. When evaluating the accuracy of the method the focus is on studying if the interaction model improves the predictions compared to not considering interaction.

1.3 Thesis Disposition

Following the introductional material, Chapter 2, *Test Case and Defenitions*, presents the WPS test case and establishes the definitions used throughout the thesis. The proposed aerodynamic method ISILL and its development is described in Chapter 3, *Aerodynamic Interaction Method ISILL*. Chapter 4, *Validation Study I: ISILL against CFD Simulations*, presents the first validation study, where the method is compared to full-scale CFD simulations. This chapter also introduces and evaluates a possible correction of the method. Chapter 5, *Validation Study II: ISILL against Wind Tunnel Tests*, presents the second validation study, where a comparison to wind tunnel test data is made. In both validation chapters, results are presented and analyzed. The results from both studies are further discussed and related to previous work in Chapter

6, *Discussion*. This chapter also includes recommendations for further studies. The main conclusions and answers to the research questions are presented in Chapter 7, *Conclusions*.

1.4 Included Publications and Author's Contribution

The material presented in Chapters 2–4 is to a large extent directly drawn from Paper I, of which the author of this thesis was the main author; that is, was main responsible for conducting the study, for code development and for writing the manuscript. Parts of Chapters 1 and 6 also include adapted material from Paper I.

The study presented in Chapter 5 uses data from the wind tunnel test campaign first reported in Paper III. The author of this thesis participated in the planning and conduction of the tests but was not the project manager and not the main author of Paper III. However, all the material presented in the validation study in Chapter 5, was produced and written specifically for this thesis and has not been published previously.

No material from Paper II is directly included in this thesis, as it presents a pre-study with preliminary results later covered in Paper I.

Chapter 2

TEST CASE AND DEFINITIONS

2.1 Introduction

In this chapter, Section 2.2 presents the full-scale test case used in this thesis. This is followed in Section 2.3 by general definitions that support upcoming chapters. Section 2.4 includes a brief discussion of why it is necessary to include viscous effects when establishing the maximum driving force generated by a WPS.

2.2 Full-Scale Test Case Geometry

The WPS used as a test case in this thesis is based on the Oceanbird research project (2018–2022), where Wallenius Marine, SSPA and the KTH Royal Institute of Technology developed a concept for a wind-powered car carrier. An early conceptual design of Oceanbird utilizing a WPS with several wingsails standing in a row is shown in Figure 1.1.

The wingsails used in the validation studies have a slightly simplified planform compared to the conceptual design; see the left-hand side of Figure 2.1. The section shape is a NACA0015 airfoil with a slightly modified, thinner trailing edge. The wingsail geometry is equal to that of the validation case that Persson et al. (2019) used when developing the SILL method. Each sail has a geometric planform area (S) of 1,844 m^2, an average chord length (c) of 23.0 m and an aspect ratio (AR) of 3.47. The sails stand in a row at the ship's centerline with an equal leading edge distance (d) of 43.2 m, which is 1.88 times the mean chord length. The center of rotation is fixed at the quarter-chord (i.e., 25% of the sail chord from the leading edge). The geometry characteristics are summarized in Table 2.1.

The sails are numbered from the foremost sail aftwards, that is, sail 1 is the sail standing in the bow. Cases with three and four sails standing in rows were tested in the validation studies. In all the calculations, the sails are assumed to stand on an infinite flat plate, which is treated as a symmetry plane.

Table 2.1: Geometry characteristics for the full-scale test case.

Sail height	80 m
Average chord	23.0 m
Area (single sail)	1,844 m^2
Aspect ratio	3.47
Sail to sail spacing	43.2 m

The material in this chapter is, with minor adaptions and additions, extracted from Paper I; see the List of Publications.

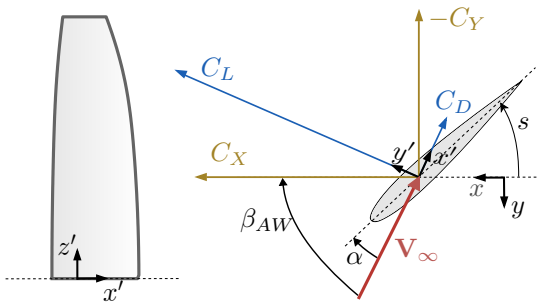

Figure 2.1: Definitions of the coordinate systems, force vectors, apparent wind angle β_{AW}, angle of attack α and sheeting angle s. The apparent wind is indicated by the red arrow.

2.3 Definitions and Coordinate Systems

Several concepts applied throughout the thesis are defined in Figure 2.1. Two coordinate systems are used. The first, the xyz coordinate system, is related to the ship's longitudinal direction and has its origin at the midpoint between the rotation centers of the sails. The y axis is positive to port and the x axis is positive forwards. The origin is at the midpoint between the rotation centers of the first and last sails (see also Figure 2.2). This point is also the assumed longitudinal center of effort (LCE) of the sails when they are equally loaded. The $x'y'z'$ coordinate system is related to each wingsail and has its origin at the quarter-chord. The x' axis is parallel to the direction of the incoming apparent wind ($\mathbf{V}_\infty$), where the infinity sign indicates undisturbed flow characteristics far upstream of the sail.

The apparent wind angle is denoted by β_{AW} and is defined as the angle between the ship's longitudinal direction and the incoming wind. In this thesis, specific apparent wind angles are sometimes translated into sailing terms where $\beta_{AW} = 15°$ and $\beta_{AW} = 30°$ correspond to sailing *close hauled*, $\beta_{AW} = 60°$ corresponds to *open reach* and $\beta_{AW} = 90°$ corresponds to *beam reach*. The angle of attack (α) is defined as the angle between the apparent wind and the chord line of the sail's profile. The local angle of attack is denoted by α_{loc}, where the subscript *loc* is used to indicate local flow conditions due to interaction effects caused by surrounding sails. The sheeting angle of a sail is denoted by a lowercase s.

The force coefficients defined in Figure 2.1 are the lift force coefficient (C_L), the drag force coefficient (C_D), the driving force coefficient (C_X) and the side force coefficient (C_Y). All the force coefficients are defined by dividing the corresponding force by $^1/_2\rho V_\infty^2 S$, where ρ is the density and the sail area is replaced by the chord length in 2D. The moment coefficients are defined by dividing the moment by $^1/_2\rho V_\infty^2 S n_{sails} d$, where n_{sails} is the number of sails. The moment coefficients are calculated in relation to the ship's coordinate system, and the sail forces are assumed to apply at the quarter-chord. The force coefficients are denoted by capital letters in 3D and by lowercase letters in 2D.

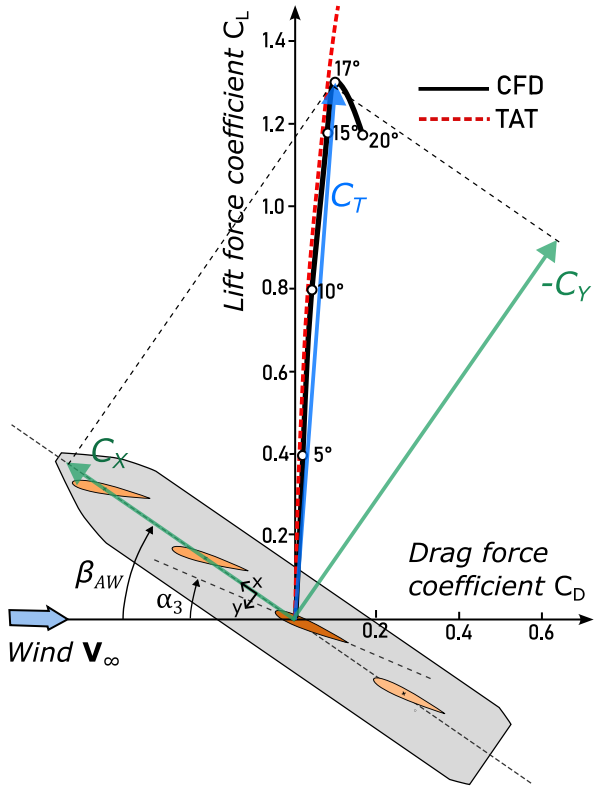

Figure 2.2: Lift coefficient C_L plotted as a function of the drag coefficient C_D, with the angle of attack as parameter. The viscous CFD curve (black) is compared to inviscid thin-airfoil theory (TAT), where $C_L = 2\pi \sin(\alpha)$ (red). The maximum total force coefficient C_T, driving force coefficient C_X and side force coefficient C_Y are indicated by arrows. Directing the driving force in the ship's longitudinal direction is an approximation.

2.4 Maximum Driving Force and Stall Prediction

The importance of stall prediction in determining the maximum driving force is illustrated in Figure 2.2. In the figure, the lift coefficient C_L for sail 3 is plotted as a function of the drag coefficient C_D, with α as parameter. The black line corresponds to the C_L/C_D curve based on viscous 3D CFD simulations for a single sail and the red dotted line is the same curve based on an inviscid model.

The total force coefficient, C_T, generated by the wingsail is indicated with a blue arrow. Because the drag force is directed in the undisturbed wind direction $\mathbf{V}_\infty$, the ship, sailing at a given apparent wind angle β_{AW} relative to the wind, can be included in the figure, and the total force can be split into driving and side forces.

As seen in the figure, the maximum driving force is achieved just before the wingsail stalls according to the 3D CFD computation. This occurs at $\alpha \approx 17°$. After

this critical α, the driving coefficient C_X decreases. The figure also includes the results from a potential flow solution according to thin-airfoil theory (see Katz and Plotkin, 2001) where there is no maximum. Although the correlation with CFD is quite good up to stall, the lack of a maximum means that potential flow methods cannot be used for wingsails in normal operating conditions, as they cannot predict the maximum driving force.

It can be noted that the ship's leeway angle has not been considered in Figure 2.2, since it is unknown. Throughout this thesis, the driving force is assumed to be acting in the ship's longitudinal direction, which in reality is only an approximation of the ship's true sailing direction.

Chapter 3

AERODYNAMIC INTERACTION METHOD (ISILL)

This chapter presents the proposed aerodynamic method for modeling interacting sails. The single-sail code SILL (Persson et al., 2019) is extended with a potential flow based vortex model for the interaction effects between the sails. In this interaction model, the sails are represented by a system of bound and free vortices.

Section 3.1 introduces the SILL method for a single sail. This is followed in Section 3.2 by a description of the sail–sail interaction model. Section 3.3 discusses the selection of control points. Finally, the steps in the full ISILL method, which combines SILL and the interaction model, are summarized in Section 3.4.

3.1 Single-Sail Model SILL

In SILL, the sail is mirrored in the deck plane and divided spanwise into several strips. Based on each strip's local wind conditions, the corresponding local force coefficients, c_l and c_d, are obtained from pre-tabulated 2D data. This 2D data can be obtained via, for example, CFD simulations or wind tunnel tests. Based on the coefficients, the related forces acting on each strip can be calculated. As the local force components obtained from the coefficients are oriented relative to the strips' local angle of attack α_{loc}, these forces are rotated to represent the lift and the drag force relative to the average angle of attack of the sail. In the case of uniform incoming flow and no interaction effects, this step becomes superfluous. The 2D forces are then integrated over the sail and are denoted by C_L^{2D} and C_D^{2D} to indicate that they do not consider 3D effects.

The 3D C_L can be estimated from C_L^{2D} by assuming an elliptical lift distribution over the sail (Anderson, 2017):

$$C_L = \frac{C_L^{2D}}{1 + \frac{2}{AR}}. \tag{3.1}$$

Based on the lift and aspect ratio the induced drag C_{D_i} may be calculated as:

$$C_{D_i} = \frac{C_L^2}{\pi AR}. \tag{3.2}$$

The induced drag is added to the integrated viscous drag to get the total drag:

$$C_D = C_D^{2D} + C_{D_i}. \tag{3.3}$$

The material in this chapter is, with minor adaptions and additions, extracted from Paper I; see the List of Publications.

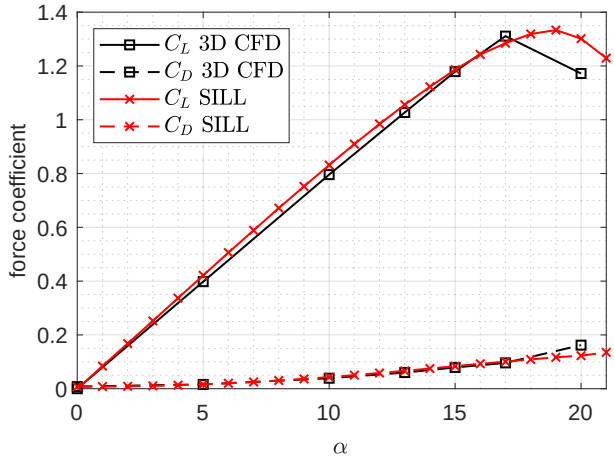

Figure 3.1: Lift and drag coefficient predictions comparing the single sail SILL model to 3D RANS CFD (Persson et al., 2019). Note that steady-state RANS simulations have limited accuracy post stall.

3.1.1 Validation and limitations of SILL

Predictions of the lift and drag coefficients for a single wingsail using SILL are presented in Figure 3.1. The test case sail is the sail described in 2. The distribution of the incoming flow is uniform and the wind speed 10m/s. In the Figure, the SILL model results are compared with 3D RANS CFD computations. The difference in the stall angle is within 2°, and the maximum lift coefficient differed by less than 1%. The drag coefficient is also well predicted.

Even though it has been shown that the SILL model can yield acceptable results for a single wingsail (Persson et al., 2019), the SILL model includes approximations, particularly the assumption of an elliptical lift distribution. In addition to possible miss-predictions of the total forces resulting from this assumption, it will also affect the prediction of the sail's point of stall. The downwash induced by the trailing vortices in 3D decrease the effective angle of attack experienced by the sail, which will to some extent also postpone the point of stall. This effect is not accounted for in the SILL model. Additionally, the validation case above assumes a uniform distribution of the incoming flow. It is possible to apply the SILL method without this assumption, but it is not tested in this thesis.

An alternative to using SILL for estimating the 3D effects on the single wing is to include the wing's own vortex system in the interaction model presented below. This approach could improve the accuracy; however, it also increases the computational cost and the risk of numerical instability. As the SILL method does not require any iterations the calculation cost is very low. The code runs in less than a second on a standard laptop.

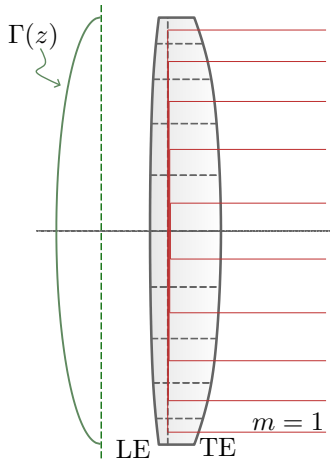

Figure 3.2: Representation of a single wingsail in the interaction model. Each sail is represented by several superimposed horseshoe vortices (red), mirrored in the deck plane at midspan. The elliptical distribution of the circulation strength $\Gamma(z)$ (green) is presented on the left. The strip index m is numbered from the bottom and up.

3.2 Sail-Sail Interaction Model

The proposed iterative sail–sail interaction model is explained below. As in SILL, each sail is discretized in strips with a corresponding horseshoe vortex, as illustrated in Figure 3.2. The vertical vortex filament of each horseshoe vortex, the *bound vortex*, is placed at the quarter-chord. The horizontal vortex part of each horseshoe vortex, the *free vortex*, is, in theory, infinitely long but has a finite length in the model. The free vortices follow the free stream direction.

An elliptical lift distribution is assumed in order to determine the strength of each vortex. Based on the total lift coefficient (estimated using SILL), the total strength of the circulation at mid sail span, Γ_0, can be calculated as follows (Anderson, 2017):

$$\Gamma_0 = \frac{2C_L|\mathbf{V}_{loc}|S}{b\pi}, \tag{3.4}$$

where $|\mathbf{V}_{loc}|$ is the average local wind strength over all strips. At midspan, the circulation strength is the sum of all bound vortices.

The total circulation strength at a strip m is calculated by:

$$\Gamma(m) = \Gamma_0\sqrt{1 - \left(\frac{2h(m)}{b}\right)^2}, \tag{3.5}$$

where h is the distance to the center of the strip from midspan. Consistent with SILL, this equation builds on the assumption of an elliptical lift distribution, also illustrated in Figure 3.2. The free vortex that originates at the intersection between two strips $m-1$ and m has the strength $d\Gamma(m) = \Gamma(m-1) - \Gamma(m)$.

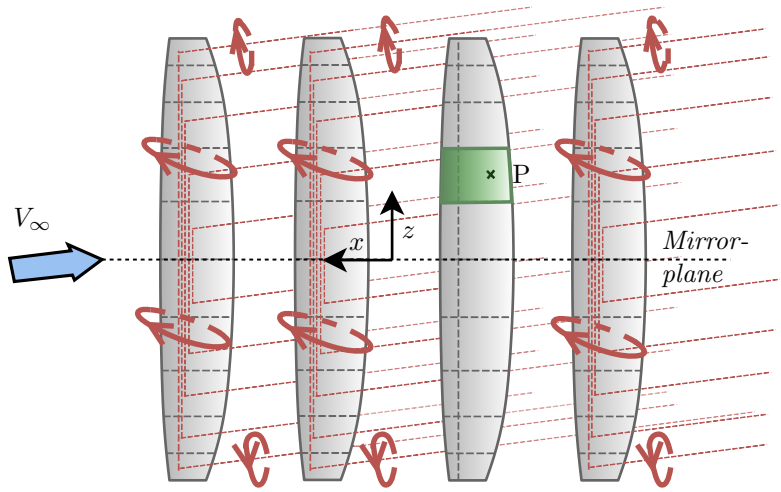

Figure 3.3: Illustration of the assumed vortex system in ISILL. The affected strip j on sail i is highlighted in green. The induced velocities generated by the bound and free vortices are illustrated with red arrows.

Modeling the sails as above, the total induced velocity from the surrounding sails on each strip j on a sail i can be calculated. This means that a local wind condition $\mathbf{V}_{loc}(i,j)$ can be determined [i.e., the global wind conditions experienced by a sail in undisturbed flow, $\mathbf{V}_\infty(i)$, plus the induced flow due to interaction, $\mathbf{V}_i(i,j)$]. The model for four sails is exemplified in Figure 3.3. According to the Biot–Savart law (Katz and Plotkin, 2001), the induced velocity $\Delta\mathbf{V}_i$ at a point P at a distance $\mathbf{r}$ from the center of a segment $d\mathbf{l}$ of a straight vortex is:

$$\Delta\mathbf{V}_i = \frac{\Gamma}{4\pi}\frac{d\mathbf{l}\times\mathbf{r}}{|\mathbf{r}|^3}, \tag{3.6}$$

where Γ is the vortex strength. By using the definitions presented in Figure 3.4 and by integration, Equation 3.6 can be modified (Katz and Plotkin, 2001, p. 38–41) to the form:

$$\mathbf{V}_i = \frac{\Gamma}{4\pi}\frac{\mathbf{r}_1\times\mathbf{r}_2}{|\mathbf{r}_1\times\mathbf{r}_2|^3}\mathbf{r}_0\cdot\left(\frac{\mathbf{r}_1}{r_1}-\frac{\mathbf{r}_2}{r_2}\right), \tag{3.7}$$

where $\mathbf{r}_0 = \mathbf{r}_1 - \mathbf{r}_2$. This form allows for calculating the induced velocity of a straight vortex segment between two points and is used in the ISILL code.

In theory, the free vortices behind the sails are of semi-infinite length, but to use Equation 3.7, they are assumed to have a finite length (longer than $400\times c$). The total induced velocity $\mathbf{V}_i(i,j)$ in a point due to interaction is calculated by summing the contributions from all bound and free vortices representing the surrounding sails. Note that the 3D effects for sail i, that is, the change in local wind angle and wind speed induced by the wake sheet behind sail i itself, has been considered following the SILL approximation and are not included when calculating $\mathbf{V}_i(i,j)$.

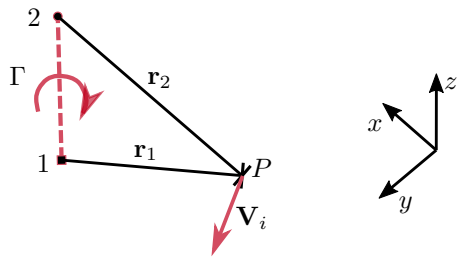

Figure 3.4: Illustration of the velocity induced in point P by a straight vortex segment with constant circulation strength Γ. The segment starts in point 1 and ends in point 2. The associated vectors $\mathbf{r}_1$ and $\mathbf{r}_1$ are used in Equation 3.7.

3.3 Selection of Control Points

As mentioned, the bound vortices are located at the quarter-chord. This is a correct choice for airfoil sections in an undisturbed flow because that is where the lift acts for thin symmetric sections. However, in a flow disturbed by other sails, this is not necessarily the best choice. To find the best position, several 2D cases with three sails were run. The effect of interaction on the pressure distribution and the position of the force center was studied. In addition, the velocity field generated by the sail using potential flow was compared with CFD for different bound vortex positions in ISILL. The conclusion was that the quarter-chord is still the best choice for the bound vortex position for airfoils in twisted flows.

When connecting the proposed interaction model with SILL, it is necessary to determine the local angle of attack. This angle is needed when obtaining local force coefficients for each sail strip from the pre-tabulated 2D data. For an airfoil in a disturbed flow, where the local velocity $\mathbf{V}_{loc}(i,j)$ changes its direction along the chord, the angle of attack is not obvious. Where should the angle be determined? Having fixed that control point, it seems natural to also use the velocity magnitude at that point to evaluate the forces from the tabulated coefficients c_l and c_d.

To evaluate the position of the control point, called $P_{i,j}$ in Figure 3.3, systematic computations with varying chordwise positions were carried out in 2D and compared to CFD. The computations showed that the most suitable position is at the three-quarter-chord (i.e., at 75% of the chord line from the leading edge). The ISILL method is sensitive to where the control point is placed. This can be seen if comparing the preliminary 3D results first presented in Paper II placing the control point at the quarter-chord to the results presented in this thesis (and in Paper I) where it is placed at the three-quarter-chord.

It can be noted that on a single airfoil in an undisturbed flow, the three-quarter-chord is also the point where the sum of the induced velocity from the bound vortex placed at the quarter-chord and the free stream velocity is parallel to the chord line (Weissinger, 1947). This means that the angle between the direction of the (theoretical) local flow at this point inside the airfoil and the free stream flow equals the airfoil's angle of attack. However, as the effect of the sail's own bound vortex

is not considered in ISILL but only the surrounding sails, the same argument for selecting the three-quarter-chord cannot be made.

When summing the forces generated at each strip, the forces need to be rotated to align them with the mean local wind angle for the whole sail. For this rotation of force vectors, the local wind condition is evaluated at the three-quarter-chord.

3.4 Full Iteration Loop

Because the SILL method requires the local wind conditions at each strip to estimate C_L and the local wind conditions are updated by the vortex interaction model, the final C_L needs to be calculated iteratively. To initiate the iterations, the induced velocities of the surrounding sails are assumed to be zero. Steps 1 and 2 below are then repeated until the induced velocities have stabilized.

1. The following steps are repeated for each sail i to establish the circulation, lift force and drag force:
   (a) For a set apparent wind angle $\beta_{AW}(j)$ and sheeting angle of sail i, s_i, the angle of attack $\alpha_{i,j}$ is calculated for each strip j.
   (b) The angle of attack is corrected by the induced velocities of the surrounding sails, calculated in Step 2. In the first iteration step, the induced velocities are 0. The new local angle of attack, $\alpha_{loc}(i,j)$, is then used to retrieve the local force coefficients in the 2D data table: $\alpha_{loc}(i,j) \Rightarrow c_l(i,j)$, $c_d(i,j)$.[1]
   (c) Following the steps in the SILL method, $C_L(i)$ and $C_D(i)$ of the 3D finite sail are estimated by integrating the 2D forces and applying the assumption of an elliptical lift distribution (Equations 3.1–3.3).
   (d) The overall $\Gamma_0(i)$ is calculated with Equation 3.4 using the sail average local wind speed $|\mathbf{V}_{loc}|$. The circulation strength at each strip, $\Gamma(i,j)$, is estimated (Equation 3.5).
2. To update the induced velocity at the point $P_{i,j}$ at the three-quarter-chord of each strip j on each sail i, the steps below are taken:
   (a) For each sail, the strengths of the horseshoe vortices representing the sail are determined based on the circulation strength established in Step 1d.
   (b) The total induced velocity, $\mathbf{V}_i(i,j)$ is calculated using Equation 3.7 by summing the contributions from all surrounding sails. The sail's own vortex system is excluded. The 3D effects on sail i are handled in Step 1c.
   (c) The new $\mathbf{V}_i(i,j)$ gives an updated local angle of attack, $\alpha_{loc}(i,j)$, and local wind speed, $|\mathbf{V}_{loc}|$, which are used as inputs in Step 1.

[1] If the boundary layer correction introduced in Section 4.3 is applied, the inviscid lift coefficient c_l^{inv} is calculated using the local angle $\alpha_{loc}(i,j)$. The interpolation between c_l^{inv} and the pre-tabulated coefficient, c_l^{tab}, is determined by Equations 4.2–4.6.

Chapter 4

VALIDATION STUDY I: ISILL against CFD Simulations

This chapter presents the validation of the ISILL method against RANS CFD simulations, both in 2D and in 3D. Also, based on the 2D results, an addition to the ISILL method that compensates for the effects of a changed boundary layer development caused by the interaction is proposed and evaluated.

The material presented in this chapter is extracted from Paper I. A pre-study on the same topic was first published in Paper II, where an earlier version of the ISILL code (then CORR-SILL) was compared to a vortex lattice method (VLM). However, no material from Paper II has been included here because the ISILL code has since been updated. No further comparison to VLMs, a true potential flow code, was deemed relevant because it is not an option for performing sheeting optimization.

The 3D CFD simulations were enabled by resources provided by the National Academic Infrastructure for Supercomputing in Sweden (NAISS) at Chalmers Centre for Computational Science and Engineering (C3SE) partially funded by the Swedish Research Council through grant agreement no. 2022-06725.

This chapter starts by describing the acquisition of CFD validation data in Section 4.1. Section 4.2 describes the validation cases. In Section 4.3, a boundary layer correction for the ISILL method is proposed and described. The results for both versions of the code, ISILL and ISILL+BL, are presented and analyzed in Section 4.4.

4.1 Description of CFD Simulations

In this study, CFD simulations are used in two ways: (1) as 2D input c_l/c_d data to SILL/ISILL and (2) as validation for ISILL. Verification and validation computations were also carried out for the CFD settings. An overview of the different CFD simulations is presented in Table 4.1. First, single-profile computations were carried out in 2D for CFD verification and validation. This step was followed by generating a c_l/c_d-table for model input. Simulations with three profiles were used to validate the ISILL method in 2D. The CFD settings in 3D were verified for one sail, then followed by simulations with four sails.

All the simulations were run with Simcenter STAR-CCM+ (Siemens, 2022) using the steady RANS equations together with Menter's k-ω shear stress transport (SST) model. The mean Reynolds number was $\approx 15 \times 10^6$. In general, the accuracy of RANS CFD simulations is limited beyond stall, and the absolute values of the forces when the sail is fully stalled can be expected to have high uncertainty.

The CFD grid verifications were performed using the numerical uncertainty analysis tool provided by MARIN, based on studies by Eça and Hoekstra (2014) and Eça et al. (2019).

The material in this chapter is, with minor adaptions and additions, extracted from Paper I; see the List of Publications.

Table 4.1: Overview of the RANS CFD computations used in Validation Study I. The chord length c (23 m) is used as the reference base length.

	No. of sails	**Usage**	**Domain**
2D	1	Verification of CFD	$90c \times 80c$
	1	Validation of CFD	
	1	ISILL input (c_l/c_d-table)	
	3	Validation of ISILL	
3D	1	Verification of CFD	$70c \times 52c \times 26c$
	4	Validation of ISILL	

4.1.1 2D simulations

In the 2D CFD calculations, the domain had four boundaries. The incoming wind was parallel to the top and bottom boundaries, which were treated as symmetry planes. The airfoil profiles were initially placed horizontally in the domain and then rotated around the mid-chord to the correct angle of attack. Low y+ wall treatment and the gamma transition model were used.

In Figure 4.1(a), the convergence of the lift coefficient with the grid density is presented. The step size on the horizontal axis is relative to the finest grid (Grid 1) and is defined as $[(\text{No. of cells Grid 1})/(\text{No. of cells Grid } n)]^{1/2}$. The numbers of cells in Grids 1 to 5 were: 1,119,542; 591,772; 309,864; 171,743; and 96,096. Also shown in the figure are the computed uncertainty bars for each grid. The finest grid had an uncertainty of 1.8%, but Grid 3 was deemed sufficiently accurate, with an uncertainty of 4%. For the viscous drag, c_d, the resulting numerical uncertainty for Grid 3 was 17.5%. This is a large uncertainty and was caused by the fact that the verification was carried out at $\alpha = 15°$, which is close to stall. However, the viscous c_d is at least one order of magnitude smaller than c_l and has little effect on the driving force c_x.

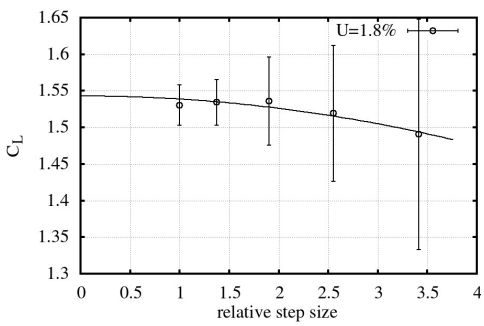

(a) Grid convergence for c_l at $\alpha = 15°$ for the 2D simulations. Grid 3, with a relative step size of 1.90, was used in the calculations.

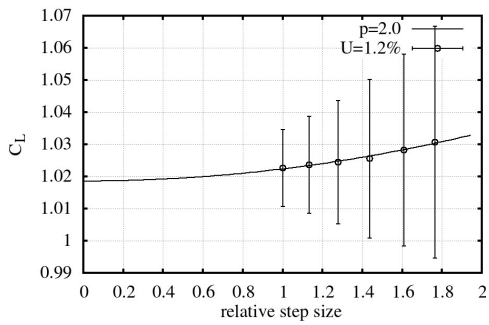

(b) Grid convergence for C_L at $\alpha = 13°$ for the 3D simulations. Grid 3, with a relative step size of 1.28, was used in the calculations.

Figure 4.1: Results of the grid verification studies. The uncertainties indicated in the figures are for the finest grid.

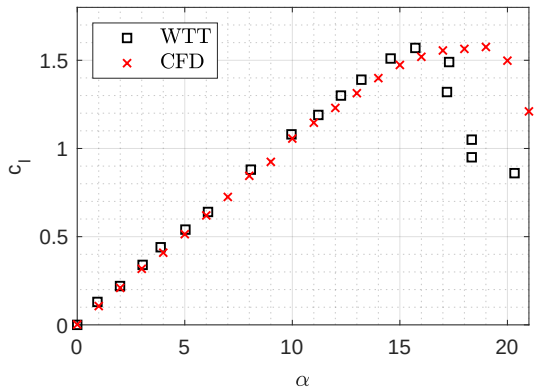

Figure 4.2: The 2D CFD simulations compared to wind tunnel tests (WTT) (Abbot and Doenhoff, 1959) at Re $= 9 \times 10^6$ for NACA0012.

The CFD computations were validated against 2D wind tunnel data presented by Abbot and Doenhoff (1959); see Figure 4.2. The profile is a NACA0012 tested at a Reynolds number of 9×10^6. The NACA0012 profile was selected because wind tunnel data for NACA0015 was not available at a Reynolds number high enough. The validation corresponds well in maximum lift, but the stall angle is overpredicted by 3°. This is deemed acceptable, especially considering that the same 2D CFD setup is used for input to the aerodynamic method ISILL and for the 2D validation. As long as the overprediction is consistent, it will not affect the validation of the aerodynamic interaction method.

The same setup as for a singe profile was used for the 2D validation cases with three profiles. The selected mesh had a maximum surface cell size of $0.0025c$ at the profile and 36 prism layers. The area between the profiles was refined to a maximum cell size of $0.025c$ and the entire mesh consisted of approximately 390,000 cells.

4.1.2 3D simulations

In the 3D simulations, the domain had six boundaries and the sail was placed vertically inside the domain. The top and bottom (floor) of the domain were set as symmetry planes and the four sides were set as velocity inlets and pressure outlets. A high y+ wall treatment was used. No transition model was used.

The grid verification, presented in Figure 4.1(b), resulted in a numerical uncertainty of 1.9% for C_L and 5.4% for C_D for the selected Grid 3. The step size on the horizontal axis is relative to the finest grid (Grid 1) and is defined as [(No. of cells Grid 1)/(No. of cells Grid n)]$^{1/3}$. The numbers of cells in the grids from Grid 1 to Grid 5 were: 25,424,790; 17,450,590; 12,194,230; 8,565,199; and 6,090,272.

The same setup was used for the 3D validation cases of ISILL with four sails. Eleven prism layers were used, and there were several refinement areas, shown in Figure 4.3. The four sail simulations had a mesh with approximately 43,000,000 cells.

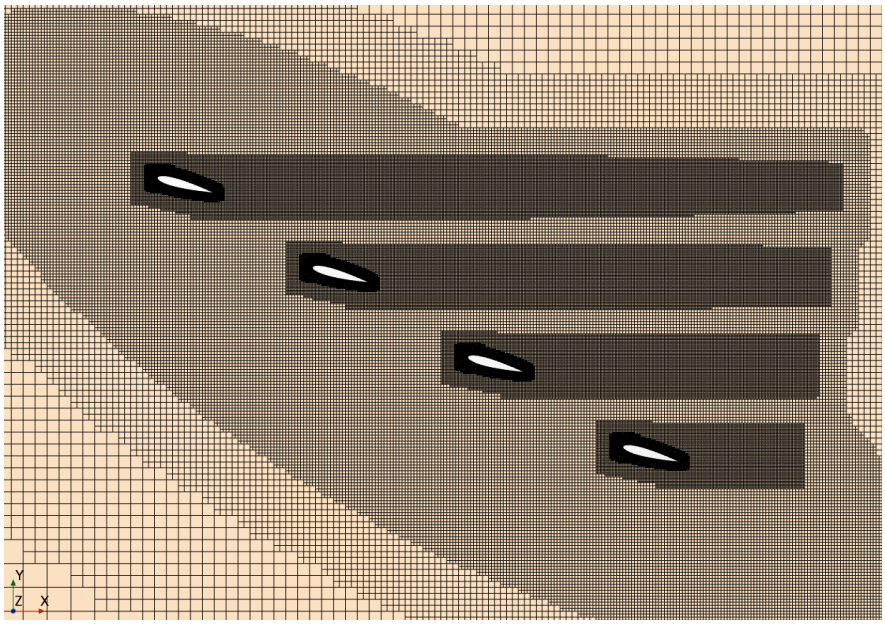

Figure 4.3: An example of the 3D mesh for four sails in a plane at $z = 75$ m, just below the tip of the wingsail.

4.2 Validation Cases

Table 4.2 gives an overview of the setup of the different validation cases. The ISILL model was evaluated both in 2D, with three profiles in a row, and in 3D, with four wingsails in a row.

The study in 2D was performed because the interaction effects in the $xy-$plane were the strongest and because it isolated the interaction of the bound vortices. By limiting the simulations to 2D, it is possible to perform multiple CFD simulations at a low computational cost. This allows performing sheeting sweeps with an increasing angle of attack, from pre- to post-stall. Simulating only three interacting profiles was selected since it was the smallest number of sails that still captured the effect on the middle wing from both an upwind and a downwind sail.

Three different apparent wind conditions were studied: (1) sailing upwind close-hauled at $\beta_{AW} = 30°$; (2) sailing upwind on a close reach at $\beta_{AW} = 60°$; and (3) beam reach at $\beta_{AW} = 90°$. The apparent wind speed (V_∞) was set at 10 m/s. The incoming free-stream wind flow was assumed to have been uniform, and the effect of the hull was not considered.

Table 4.2: Test matrix defining the different validation cases (v.c.) in Validation Study I. The italicized letters indicate that the angle of attack is swept over a span of angles.

	v.c.	β_{AW}	α_1	α_2	α_3	α_4
2D	2.1	30	*11–17*	19	22	
	2.2	30	15	*15–23*	20	
	2.3	30	16	19	*13–27*	
	2.4	60	*11–20*	19	19	
	2.5	60	18	*15–23*	19	
	2.6	60	18	19	*13–25*	
	2.7	90	*11–22*	19	19	
	2.8	90	19	*15–23*	19	
	2.9	90	19	19	*13–23*	
3D	3.1	30	15	15	15	15
	3.2	60	15	15	15	15
	3.3	90	15	15	15	15
	3.4	30	15	18	20	22

4.3 Boundary Layer Effects and Postponed Stall (ISILL+BL)

When two lifting airfoils are close together such that the trailing edge (TE) of the forward foil is in the low-pressure zone on the suction side of the aft foil, the adverse pressure gradient on the suction side of the forward foil will be reduced. The boundary layer then grows more slowly and is less prone to separation. As a result, larger angles of attack may be attained before the sail stalls. Therefore, this section suggests an addition to the ISILL method that corrects for these effects. The method with this correction is called ISILL+BL.

ISILL in its basic implementation does not consider the interaction effect on the boundary layer, as it uses the local wind conditions at the control point to look up pre-calculated lift and drag coefficients. These coefficients have been established in an undisturbed environment. In upwind conditions, this causes an underprediction of the maximum lift force and stall angle. In some of the 2D validation cases presented in this chapter, the lift force on the forward sail was found to be underpredicted by approximately 10% by ISILL. This can be seen for the upwind case ($\beta_{AW} = 30°$) in Figure 4.4 when comparing the ISILL prediction to the CFD results.

The suggested addition to ISILL consists of a boundary layer correction that adjusts the 2D lift curve $c_l(\alpha)$ when the TE is near the low-pressure region of the following sail. This is done by blending a theoretical inviscid lift coefficient c_l^{inv} and the lift coefficient obtained from the pre-calculated 2D table, c_l^{tab}. The inviscid lift coefficient is based on thin airfoil theory and is calculated by

$$c_l^{inv} = 2\pi \sin(\alpha). \tag{4.1}$$

Note that this equation was used as input to SILL when producing the 3D lift curve in Figure 2.2 in Section 2.4.

As was illustrated in Figure 2.2, in inviscid potential flow theory, the sail does not stall. The stall angle and maximum lift force can therefore be increased by interpolating between the tabulated viscous c_l^{tab} and the inviscid c_l^{inv}

$$c_l = f_{tab} c_l^{tab} + f_{inv} c_l^{inv}, \tag{4.2}$$

where the relation between the fractions is $f_{tab} = 1 - f_{inv}$. However, a control mechanism for the interpolation is needed.

I is assumed that the fraction of the inviscid lift, f_{inv}, can be determined based on the change in adverse pressure gradient on a wing caused by the interaction. To obtain a metric for this change, the pressures at the TE and the three-quarter-chord are used. The difference between these pressures is a measure of the rear part's pressure gradient. By computing the change in this pressure difference due to the surrounding wings, it is possible to get a metric for the interaction effect. This metric is denoted as ΔC_{pi} and is calculated as

$$\Delta C_{pi} = C_{pi}(TE) - C_{pi}(75\%). \tag{4.3}$$

The induced pressure coefficient C_{pi} is obtained from

$$C_{pi} = 1 - \left(\frac{|\mathbf{V}_{loc}|}{|\mathbf{V}_\infty|} \right)^2, \tag{4.4}$$

where $\mathbf{V}_{loc} = \mathbf{V}_i + \mathbf{V}_\infty$. Once again, it is only the induced velocities created by the surrounding wing that are considered when calculating $\mathbf{V}_i$.

Although there are good physical reasons for a coupling between f_{inv} and ΔC_{pi}, the exact relation is unknown. To determine this, a reference case is required. In Validation Study I, an upwind case where $\beta = 30°$ and the postponed stall effect is strong is selected. f_{inv} is then adjusted to yield good correspondence (in 2D) between CFD and ISILL+BL; see Figure 4.4. Setting f_{inv}^{ref} to 0.45 gives a balanced correction, meaning that 45% of the lift coefficient comes from the inviscid c_l^{inv} and 55% from the viscous c_l^{tab}. The corresponding metric for the reference case is ΔC_{pi}^{ref}. The assumption is therefore that the f_{inv} for any case can be established by

$$\frac{f_{inv}}{f_{inv}^{ref}} = g\left(\frac{\Delta C_{pi}}{\Delta C_{pi}^{ref}} \right), \tag{4.5}$$

where g is an unknown function.

The simplest relation is a linear dependence. This yields a considerable improvement in the prediction of maximum c_l and the corresponding stall angle. However, the connection appears to be stronger, and therefore a quadratic dependence was tested. The results were then further improved, and the following relation was adopted:

$$\frac{f_{inv}}{f_{inv}^{ref}} = \left(\frac{\Delta C_{pi}}{\Delta C_{pi}^{ref}} \right)^2. \tag{4.6}$$

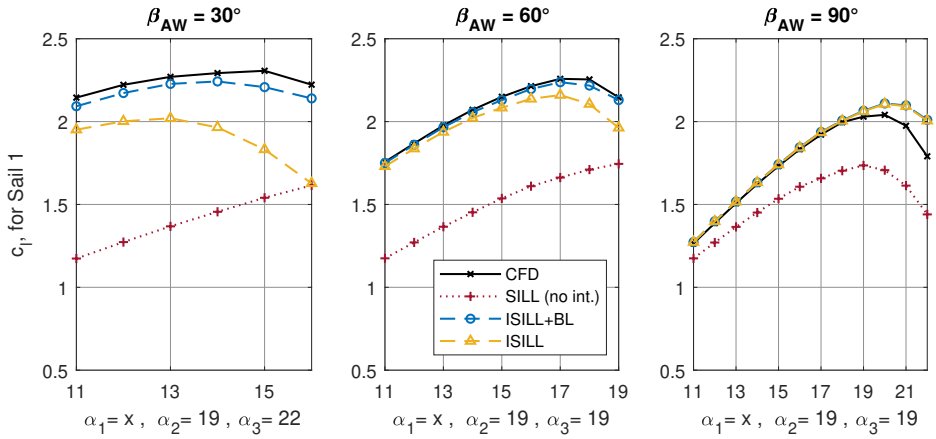

Figure 4.4: Lift coefficient for Sail 1 when sailing at $\beta_{AW} = 30$ (v.c. 2.1), $\beta_{AW} = 60$ (v.c. 2.5) and $\beta_{AW} = 90$ (v.c. 2.7). The forward profile (Sail 1) is swept from a low to a high angle of attack, whilst the other two profiles are kept stationary.

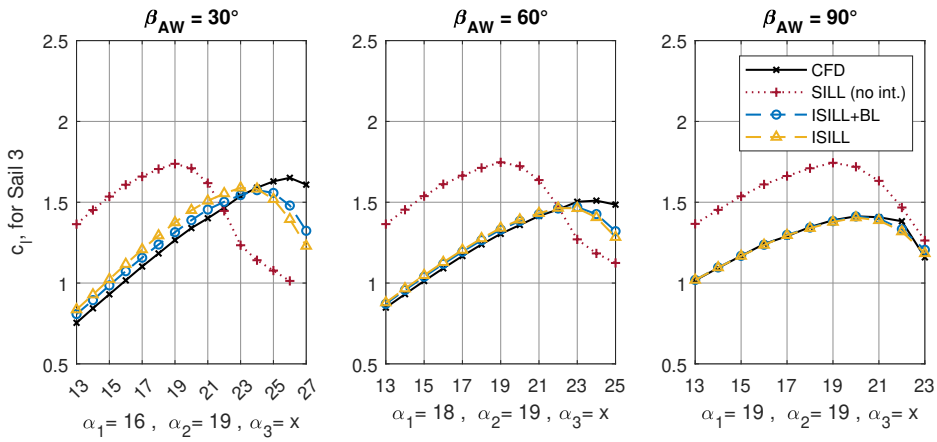

Figure 4.5: Lift coefficient for Sail 3 when sailing at $\beta_{AW} = 30$ (v.c. 2.3), $\beta_{AW} = 60$ (v.c. 2.6) and $\beta_{AW} = 90$ (v.c. 2.9). The aftmost profile (Sail 3) is swept from a low to a high angle of attack, whilst the other two profiles are kept stationary.

To avoid unrealistic corrections, f_{inv} is limited to the range 0.0–0.45 and the change in stall angle due to the correction is limited to a maximum of 5°. The correction reference values, C_{pi}^{ref} and f_{inv}^{ref}, have been calibrated in 2D. The same reference values are applied in 3D.

Figures 4.4 and 4.5 present the results for a 2D angle sweep with Sail 1 and Sail 3 [see Table 1 (validation cases 2.1, 2.3, 2.4, 2.6, 2.7 and 2.9)]. The method's predictions with (ISILL+BL) and without (ISILL) boundary layer correction and the

computation without interaction (SILL) are validated against CFD results. There is a large improvement in the predictions even without boundary layer correction; but when this correction is included, a further improvement is noted for the upwind cases. At $\beta_{AW} = 90°$, there is no correction, as the trailing edges of the forward wings are away from the low pressures of the following sail.

4.4 Results and Analysis

In this section, the results are presented and discussed. The results from the 2D stall validation study are presented first, followed by the 3D validation results.

4.4.1 2D stall study - sheeting sweep for different β_{AW}

Figures 4.6–4.8 present the total 2D forward driving force coefficient and yaw moment coefficient for the 2D validation cases in Table 4.2. The method's predictions without (ISILL) and with (ISILL+BL) boundary layer correction are compared with the CFD results and the results using SILL, which does not consider the interaction effects. In each figure, one of the three sails is swept from a low to a high angle of attack past the optimal sheeting angle where the maximum driving force is generated. The other two sails are fixed, set at sheeting angles close to the maximum lift force so that these

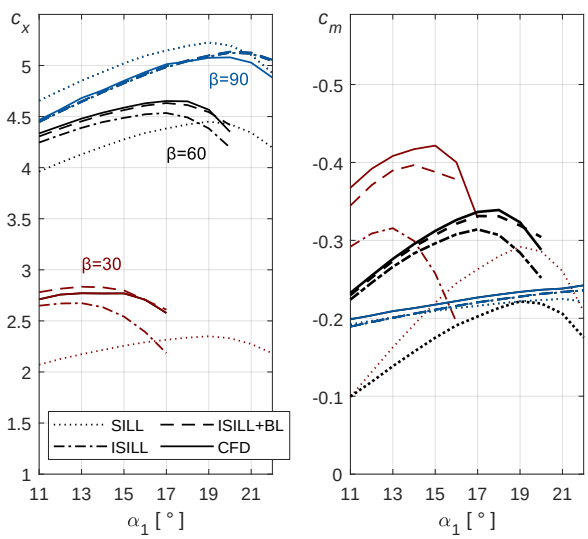

(a) Driving force coefficient (b) Yaw moment coefficient

Figure 4.6: 2D sheeting sweep for $\beta_{AW} = 30°$, 60° and 90° where Sail 1 (fore) is swept from a low to a high angle of attack. For sheeting angles of Sail 2 and Sail 3; see validation cases 2.1, 2.4 and 2.7 in Table 4.2.

two stationary sails will generate a strong interaction effect, altering the velocity field around the sweeping sail.

In the figures, the blue lines show the results for the ship sailing at an apparent wind angle of 90°; the black lines for 60°; and the red lines for 30°. All the CFD results are presented with full lines; the ISILL results with dash–dotted lines; the ISILL+BL results with dashed lines; and the SILL results with dotted lines.

Studying the difference between ISILL and SILL, that is, with and without considering interaction, the difference increases when the ship points higher toward the wind. Sailing upwind also generates the largest differences in moments. The highest driving force is generated for beam reach ($\beta_{AW} = 90°$).

For all test cases, the interaction model improved the prediction of the driving force coefficient. The model improves both the predicted absolute value and angle of attack for which the maximum c_x is reached. The largest effects of the interaction are seen in the two upwind cases ($\beta_{AW} = 30°$ and $\beta_{AW} = 60°$), which ISILL+BL predicted. In general, ISILL without compensating for the boundary layer effects also improves the prediction of the driving force around stall compared to SILL but not as much as ISILL+BL. The prediction of the force at beam reach is good, but this is also the condition with the weakest interaction effects. There are some deviations from the CFD results of the driving force curve for the sweep with Sail 2 in upwind sailing, as seen in Figure 4.7(a). For this middle sail, some of the interaction effects from the sail in front and the sail behind cancel each other out, but the flow still

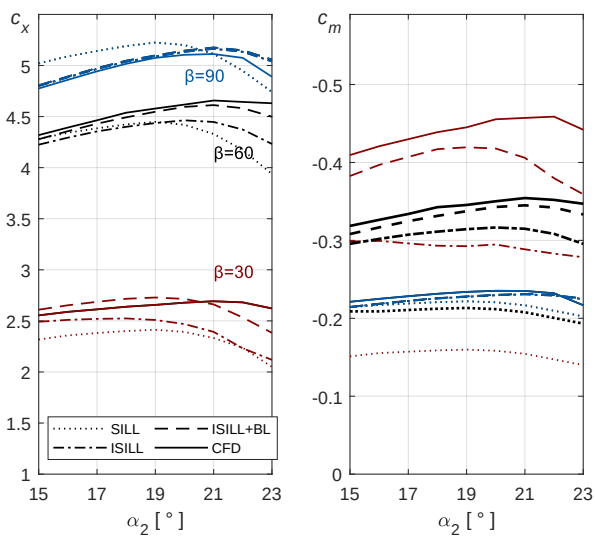

(a) Driving force coefficient (b) Yaw moment coefficient

Figure 4.7: 2D sheeting sweep for $\beta_{AW} = 30°$, 60° and 90° where Sail 2 (mid) is swept from a low to a high angle of attack. For sheeting angles of Sail 1 and Sail 3; see validation cases 2.2, 2.5 and 2.8 in Table 4.2.

differs considerably compared to a sail in undisturbed flow. In Figure 4.6(a) and Figure 4.8(a) presenting the sweeps with the forward sail and the aft sail, it is clear that the interaction has a strong effect on the location of the maximum c_x for these cases, shifting it by several degrees.

The yaw moment in the upwind cases is strongly affected by the interaction effect in all three sweeps, with the overall load center shifting forward because the lift force generated by the foremost sail increases and the force on the aftmost sail decreases. As seen in Figure 4.7, even when the change in the total driving force due to the interaction is relatively small, the effect on the yaw moment in upwind conditions can be large. This effect is captured both by ISILL and ISILL+BL. However, without the boundary layer correction, the loads on the foremost sail are underestimated, resulting in a too low yaw moment in the upwind cases. Studying the moments for $\beta_{AW} = 30°$ in Figure 4.6(b), it can be seen that the difference between the results without considering interaction effects (SILL) and the results from CFD are large. This shift in the center of longitudinal effort has important implications for the ship's maneuverability. In addition, from Figure 4.6(b), it is apparent that sheeting in the foremost sail, thus increasing α_1 and the load on Sail 1, the absolute yaw moment will increase until the sail stalls. The opposite effect on yaw moment is seen in Figure 4.8(b) when sheeting in the aftmost sail. The ISILL+BL method provides very good prediction of this behavior.

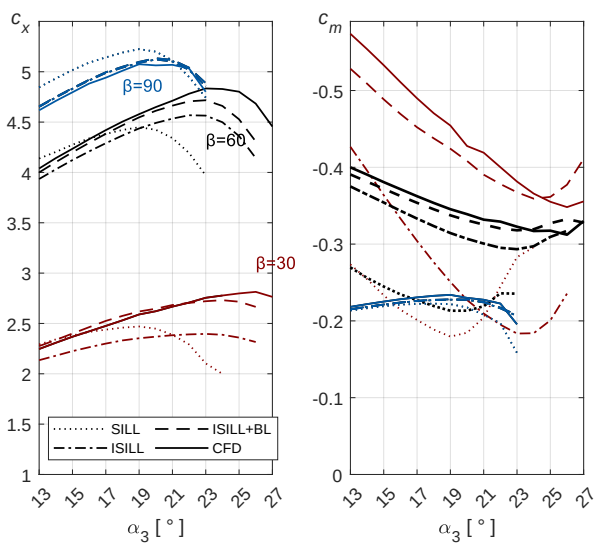

(a) Driving force coefficient (b) Yaw moment coefficient

Figure 4.8: 2D sheeting sweep for $\beta_{AW} = 30°$, 60° and 90° where Sail 3 (aft) is swept from a low to a high angle of attack. For sheeting angles of Sail 1 and Sail 2; see validation cases 2.3, 2.6 and 2.9 in Table 4.2.

4.4.2 Four sails with fixed sheeting in 3D

Figures 4.9–4.11 present the validation cases 3.1, 3.2 and 3.3, defined in Table 4.2. In each of these validation cases, all four sails are sheeted equally to an angle of attack of $\alpha = 15°$. The driving and side force coefficients are shown for the four sails. Because the sails are sheeted equally in each figure, when using SILL and not considering interaction, all four sails generate an equal force. Considering interaction, there is generally a large variation in forces between the sails. The figures show the results with (ISILL+BL) and without (ISILL) the boundary layer correction.

Figure 4.9 (validation case 3.1) shows the results when the ship is sailing upwind close-hauled with $\beta_{AW} = 30°$. Consistent with the 2D results, strong interaction effects can be observed for this upwind case. The moments are not presented explicitly, but the figure shows how the load changes drastically from fore (Sail 1) to aft (Sail 4) due to the interaction. Both versions of ISILL predict this change. There is little difference between the two versions because the foremost sails are not close enough to their stalling points for the correction to have any effect. The negative effect on the downwind sails (Sails 2–4) is somewhat underestimated, resulting in a small overprediction of the forces.

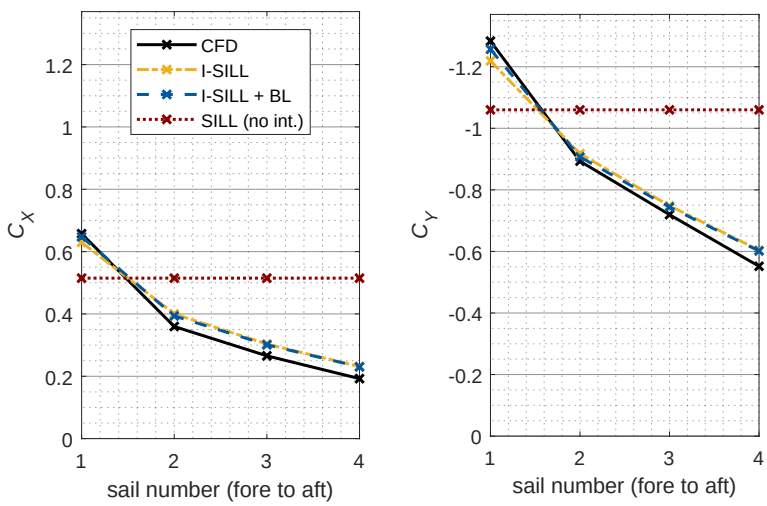

(a) Driving force coefficient

(b) Side force coefficient

Figure 4.9: Total force coefficients for $\beta_{AW} = 30°$ when all the sails are equally sheeted to $\alpha = 15°$ (validation case 3.1).

Figure 4.10 (validation case 3.2) shows the results for an apparent wind angle of $\beta_{AW} = 60°$, corresponding to close reach. The forces are well predicted on all sails for this validation case. Figure 4.11 (validation case 3.3) presents the force coefficients when the ship is sailing on beam reach. Here, the forces on the upwind sails (Sail 1–3) are slightly overestimated, especially the side force seen in Figure 4.11(b), which for $\beta_{AW} = 90°$ is equal to the predicted C_D. In this case, the SILL model without interaction actually corresponds better to the CFD results, but the difference is small.

In Figure 4.12 (validation case 3.4), the sheeting angles have been adjusted to better represent realistic sheeting in an upwind case. By decreasing the sheeting angles on the downwind sails, the interaction effect increases and the front sail has begun to reach its maximum lift before stalling. A difference between ISILL and ISLL+BL can bee seen for this case. The boundary layer correction slightly improves the predicted loads. By sheeting in and increasing the load on the downwind sails (compare, e. g., Sail 2 in Figure 4.9 and Figure 4.12), the local angle of attack for Sail 1 has increased.

As expected, the total driving force decreases and the side force increases as the ship points closer to the wind. In each validation case, it can also be seen that the total driving force predicted by ISILL is lowered due to the interaction, and one could draw the conclusion that the interaction effect is always unfavorable in terms of generated driving force. However, with the more optimized sheeting, as presented in Figure 4.12, the driving force is improved. Through proper optimization of the sheeting angles, the driving force would be even higher.

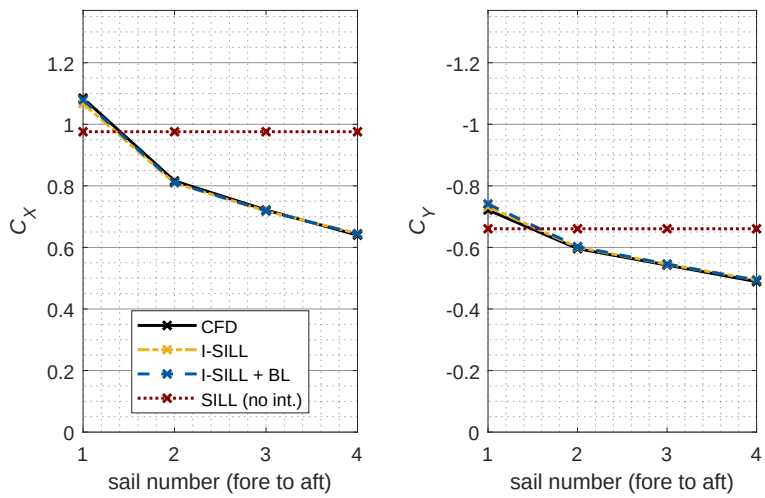

(a) Driving force coefficient

(b) Side force coefficient

Figure 4.10: Total force coefficients for $\beta_{AW} = 60°$ when all the sails are equally sheeted to $\alpha = 15°$ (validation case 3.2).

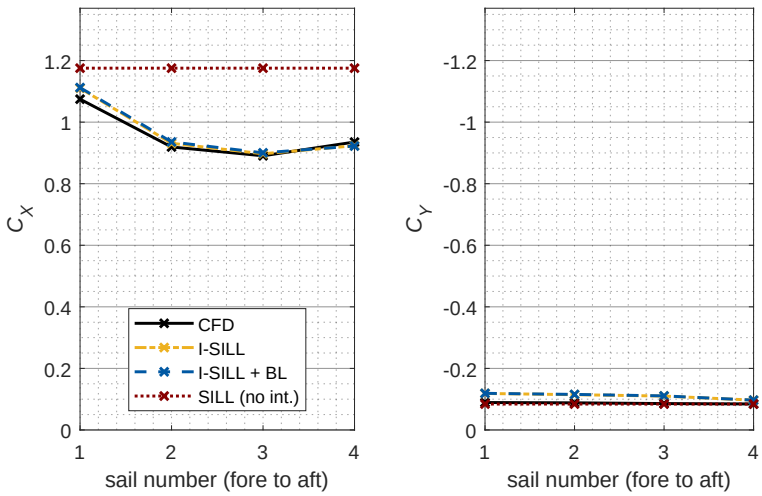

(a) Driving force coefficient (b) Side force coefficient

Figure 4.11: Total force coefficients for $\beta_{AW} = 90°$ when all the sails are equally sheeted to $\alpha = 15°$ (validation case 3.3).

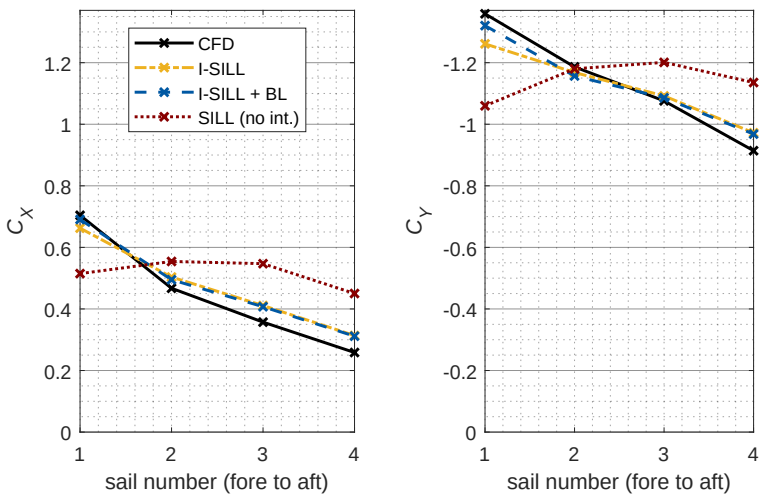

(a) Driving force coefficient (b) Side force coefficient

Figure 4.12: Total force coefficients for $\beta_{AW} = 30°$ when the sails are sheeted to $S_1 = 15°$, $S_2 = 12°$, $S_3 = 10°$ and $S_4 = 8°$ (validation case 3.4).

Chapter 5

VALIDATION STUDY II: ISILL against Wind Tunnel Tests

This chapter presents the validation of the ISILL method (without the boundary layer correction proposed in Chapter 4) against wind tunnel tests. The wind tunnel test campaign was conducted as part of the Oceanbird research project.

The experiments were performed in the R.J. Mitchell wind tunnel at Southampton University, a closed-circuit wind tunnel with cross-section dimensions of 3.5 m $\times$ 2.4 m. The tests were partly planned and conducted within this licentiate project in 2021, and the experimental results were first presented in a conference paper by Marimon Giovannetti et al. (2022). A subset of the results from the experiments is used for the wind tunnel validation study presented in this thesis.

5.1 Experimental Setup

In the wind tunnel tests, a setup with only three wingsails was tested to minimize blockage effects while still maintaining complex interaction effects. The model sails corresponded to a scale of 1:58 compared to the full-scale test case, described in Chapter 2. The dimensions of the model are summarized in Table 5.1.

The three sails were mounted in a row hanging from the tunnel roof balance, as illustrated in Figure 5.1. The profile of the sails was a NACA0015 section, and the planform was as defined in the full-scale test case. Each sail rotated at 25% of the chord (quarter-chord). Different apparent wind angles (β_{AW}) corresponding to the ship sailing at different angles relative to the wind were achieved by rotating the roof balance. The overall forces were measured with a six-component Nuntem load cell balance. The individual forces and moments of each sail were also measured with separate transducers. Thin sheets of foam plastic were added to the tunnel roof to ensure that no gap between the bottom of the sails and the roof remained.

The incoming wind speed was set to 25 m/s. This resulted in a Reynolds number of 7.62×10^5, based on the maximum chord length, which is within the flow regime where laminar boundary layer effects may be substantial. To try to ensure transition

Table 5.1: Geometry characteristics of the wind tunnel scale model

Number of sails	3
Span	1385 mm
Average chord	400 mm
Maximum chord	460 mm
Area (single sail)	0.552 m^2
Aspect ratio	3
Mast to mast spacing	748 mm

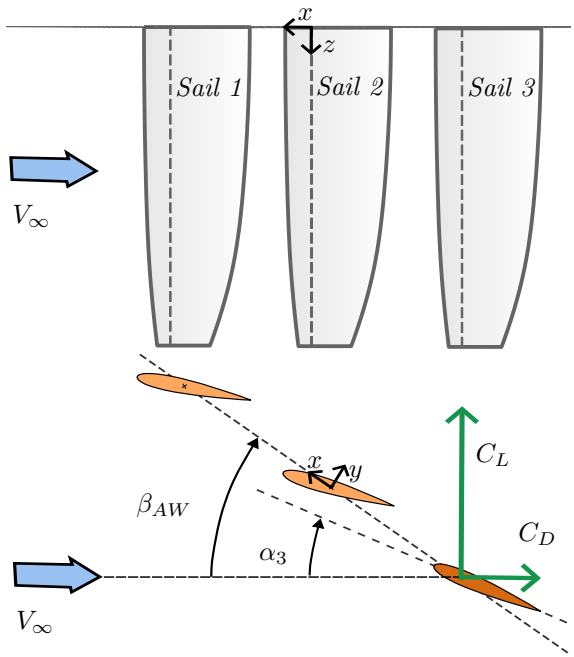

Figure 5.1: Top (below) and side (above) view of the wingsails in the experimental setup. The incoming wind (V_∞) is indicated with arrows. The apparent wind angle (β_{AW}), the angle of attack for Sail 3 (α_3), the lift coefficient (C_L) and the drag coefficient (C_D) are defined. The origin of the model's coordinate system is at the quarter-chord of Sail 2.

to the turbulent flow regime, a zigzag transition tape was placed at the quarter-chord on both sides of each sail. The wind tunnel turbulence intensity levels have been reported to be less than 0.2% (Castro, 2001).

Due to mechanical load limits, it was not possible to rotate the sails whilst maintaining a constant speed of 25 m/s.Therefore, tests with angles of attack over approximately 17°–19° had to be performed by lowering the wind speed to 10 m/s before rotating the sails and then after setting the new sheeting angles increasing the speed back to 25 m/s. Results from the wind tunnel tests showed that lowering and ramping up the speed generated a hysteresis effect, where the sails stalled at lower angles of attack. Therefore, the test results were divided into two groups, one where the wind speed was kept constant throughout a test series and one where the speed was lowered and ramped up. In the present study, only tests performed at a constant speed of 25 m/s have been selected as validation cases.

In the experiments, the effect of blockage was not established. Blockage effects are a know problem in wind tunnel testing and are discussed by, for example, Barlow et al. (1999). Buoyancy blockage and wake blockage can be assumed to be small and/or compensated for. However, effects caused by solid blockage and the streamline

Table 5.2: Selected validation cases. The angle of attack for each sail is indicated. For validation cases $T9$–$T29$, the matrix was repeated for $\beta_{AW} = 15°$, $30°$, $60°$ and $90°$. $S4$–$S16$ were run at $\beta_{AW} = 30°$.

Case	Sail 1	Sail 2	Sail 3
T9	0	5	10
T10	3	5	7
T11	4	5	6
T12	5	5	5
T13	6	5	4
T14	10	5	0
T15	3	5	12
T16	7	5	7
T17	5	10	15
T18	8	10	12
T19	9	10	11
T20	10	10	10
T21	11	10	9
T22	15	10	5
T23	8	10	17
T24	12	10	12
T25	10	15	20
T26	13	15	17
T27	14	15	16
T28	15	15	15
T29	16	15	14

Case	Sail 1	Sail 2	Sail 3
S4	13	0	17
S5	13	5	17
S6	13	10	17
S7	13	11	17
S8	13	12	17
S9	13	13	17
S10	13	14	17
S11	13	15	17
S12	13	16	17
S13	13	17	17
S14	13	18	17
S15	13	19	17
S16	13	20	17

curvature correction could be significant. Unfortunately, standard correction formulas for one sail cannot be applied to quantify these effects, sand hence CFD calculations or potential flow-based calculations with mirror images in the tunnel walls would be needed. In general, the solid blockage causes an increased wind speed, and the effect is stronger closer to the tunnel walls. The streamline curvature correction leads to an increased local angle of attack experienced by the model sails. Both effects increase the generated forces on the sails, especially for the validation cases with higher apparent wind angles, where Sail 1 and Sail 3 are closer to the tunnel walls.

5.2 Validation Cases

The sheeting test matrix for the selected validation cases is presented in Table 5.2. For validation cases $T9$–$T29$, the sheeting was determined by setting the middle sail to a fixed angle of attack and then systematically varying the sheeting of the front and aft sail. The fixed angle of attack of the middle sail started at $\alpha_2 = 0°$ and was increased to $\alpha_2 = 15°$ in steps of $5°$. The tests at $\alpha_2 = 0°$ have been excluded here due to very small loads. A set of validation cases with the same fixed angle of attack for the middle sail are below referred to as a group, where Sail 2 set to $5°$, $10°$ and $15°$

corresponds to groups 1, 2 and 3. The validation cases $T1$–$T29$ were each tested in a series, keeping the wind speed constant. The tests were repeated for four different apparent wind angles.

Additional tests, $S4$–$S16$, were performed where the middle sail was swept from $\alpha_2 = 0^\circ$ to $\alpha_2 = 20^\circ$, whilst the other two sails remained stationary at a constant sheeting angle. The angles of attack of Sails 1 and 3 were chosen based on the previous tests so that both sails would be highly loaded and generate large interaction effects. Several different apparent wind angles were tested, but the tests at $\beta_{AW} = 30^\circ$ were the only series performed at a constant wind speed.

Finally, tests were also performed for a single sail, where the forward sail and the aft sail was removed and the roof balance was set to an angle corresponding to $\beta_{AW} = 0^\circ$. The remaining sail was then swept from 0° to 20° in steps of 1°.

5.3 Single Sail Calibration

In order to apply the ISILL method, input 2D c_l/c_d-data is required. In Section 3.1, two ways of generating these 2D data were suggested, CFD simulations or wind tunnel tests. In this validation study, CFD simulations were rejected because the flow was within the transitional regime and the wingsails were equipped with zigzag transition tape, making the CFD results very sensitive to different transition modeling strategies and assumed turbulence intensity levels.

Instead, 2D wind tunnel test results were evaluated as input. However, no 2D wind tunnel results were found for a NACA0015 section at the correct Reynolds number using zigzag transition tape at the quarter-chord. Bertagnolio (2008) performed wind tunnel tests at $Re = 1.6 \times 10^6$ without transition tape/strips. He ran the tests with different turbulence levels in the tunnel using two different turbulence grids (with high and low solidity) and no turbulence grid. Sheldahl and Klimas (1981) also tested the NACA0015 section at $Re = 0.7 \times 10^6$. These tests were performed both with and without transition strips at 17% of the chord length, but the results were similar and only the results without strips were presented in the report.

The different 2D c_l/c_d-data discussed above are plotted in Figure 5.2. It can be concluded that the maximum lift coefficient and stall angle are sensitive to Reynolds number effects as well as turbulence level in the wind tunnel. Because the exact turbulence level in the R.J. Mitchell wind tunnel and the effect of the zigzag transition tape on the sail model are unknown, it was decided to control and calibrate the 2D input data using the 3D single-sail test results. This was done by comparing the output of the single-sail SILL model using various 2D tables as input for the single-sail test results; see Figure 5.3. The incoming flow was assumed to be uniform using the lifting-line model. The 2D wind tunnel data by Sheldahl and Klimas (1981) could have been expected to be the best input candidate because the Reynolds number was very similar to that in the tests in the R.J. Mitchell tunnel, but using it as input to the SILL model underpredicts the maximum lift by over 20%. Instead, 2D data by Bertagnolio (2008) with a high-solidity grid was selected, and any deviating points were calibrated to match the 3D SILL results. As seen in Figure 5.3, the calibration

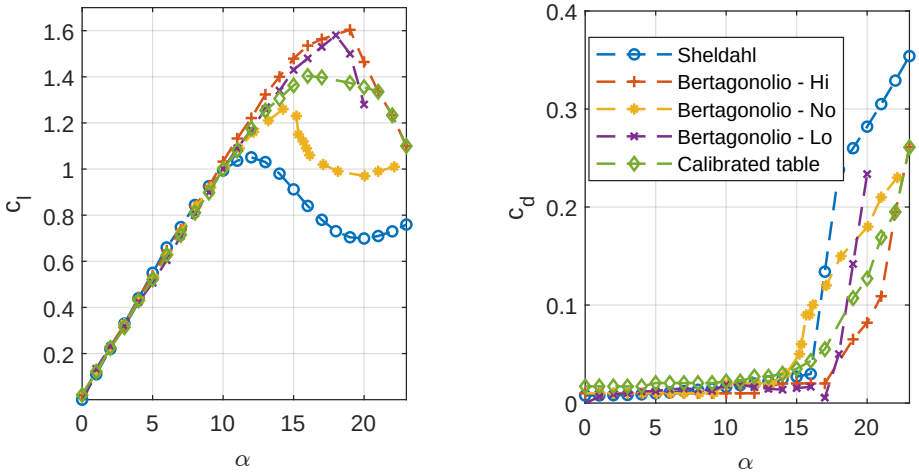

(a) 2D lift coefficient

(b) 2D drag coefficient

Figure 5.2: 2D wind tunnel data at two different Reynolds numbers, $Re = 0.7 \times 10^6$ (Sheldahl and Klimas, 1981) and $Re = 1.6 \times 10^6$ (Bertagnolio, 2008). Bertagnolio (2008) reports results with three different turbulence levels — using a high-solidity turbulence grid (Hi), a low-solidity turbulence grid (Lo) and no turbulence grid (No). The calibrated 2D input table is also presented.

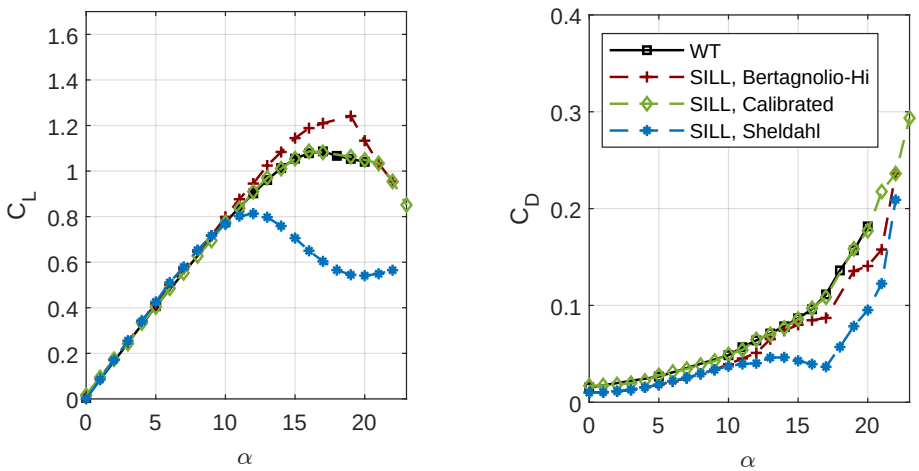

(a) 3D lift coefficient

(b) 3D drag coefficient

Figure 5.3: Wind tunnel test (WT) results for a single sail, plotted together with results from the SILL model using different input data. Three different input data are used, two 2D wind tunnel data sets by Bertagnolio (2008) and Sheldahl and Klimas (1981) and a 2D c_l/c_d-table that has been calibrated to fit the 3D wind tunnel test results.

of the c_l/c_d-table only affects the model's results at higher angles of attack.

The process of calibrating the input data for the single-sail SILL model based on 3D single-sail results is adopted in this study because the main focus is to evaluate ISILL's ability to predict sail–sail interaction effects. However, this approach may well be applicable in a practical WPS design process.

5.4 Results and Analysis

This section presents and analyses the results from the validation of the aerodynamic interaction method ISILL against wind tunnel tests. ISILL is compared both to the wind tunnel test results and the single-sail SILL model, which does not consider interaction.

In all figures in this section (Figures 5.4–5.13), the wind tunnel results are marked by black squares, the ISILL method by yellow dots and the SILL model by red crosses. The error bars for the wind tunnel data represent the standard deviation of the measurements.

Results for validation cases $T9$–$T29$ are presented in Section 5.4.1 for four different apparent wind angles. The stall study based on the sweep with the middle sail ($S4$–$S16$), is presented in Section 5.4.2.

5.4.1 Total driving force and center of effort

The results for validation cases $T9$–$T29$ (see Table 5.2) are presented here, both on an aggregated level for all cases and in detail for a few highlighted ones. The two main variables investigated are the predicted total driving force, C_X, and the position of the LCE. The results for four different apparent wind angles are presented in consecutive order; $\beta_{AW} = 15°$, $30°$, $60°$ and $90°$.

C_X is calculated according to the definitions in Figure 2.1 and Figure 2.2 and represents the force generated by the WPS in the ship's longitudinal direction. The shift in LCE is a measure of how much the three sails' combined center of effort has shifted (forward of the origin of the ship's coordinate system, i.e. forward of the rotation point of Sail 2) as seen in Figure 5.1. The distance that the LCE has shifted is normalized by dividing by the ship's length, The shift in LCE can be calculated as:

$$\text{shift in LCE [\%]} = \frac{\text{Moment around origin}}{\text{Distance Sail 1 to Sail 3} \times \text{Total side force}} \times 100, \qquad (5.1)$$

where the moment is calculated based on the side forces and the distance between the sails. When the sails are equally loaded, the shift in LCE is 0. In all calculations presented here and when post-processing the wind tunnel data, it has been assumed that the generated lift and drag forces act in the quarter-chord.

5.4.1.1 Sailing close hauled, $\beta_{AW} = 15°$ and $\beta_{AW} = 30°$

In Figure 5.4, the ship is sailing at an apparent wind angle of 15°, very close to the wind. The total driving force is therefore low because the direction of the generated lift force is almost orthogonal to the direction of the driving force. Sailing at this low apparent wind angle, the drag force's negative effect on the driving force becomes considerable. Still, the lift force projected in the ship's longitudinal direction (forwards) is more than twice as great than the projected drag force (directed afterward), and the resulting C_X is positive. In general, the difference in C_X between ISILL and the wind tunnel tests is small for this apparent wind angle, and the difference is reduced by applying the interaction model. The difference is somewhat larger for cases $T28$ and $T29$, as these validation cases appears to have started to stall in the wind tunnel tests but not using the ISILL method.

Studying the shift in LCE in Figure 5.4(b), it can be seen that there is a large variation between the different validation cases. This variation is well predicted by the ISILL method. Validation case $T14$ (displayed in detail in Figure 5.5) with angles of attack $\alpha_1 = 10°$, $\alpha_2 = 5°$ and $\alpha_3 = 0°$is the most extreme case, as the center of effort of the sails moves more than 70% forward of the origin. This is due to the sheeting, where the foremost sail generates a positive lift and a corresponding negative side force, but the middle sail and aftmost sail generates close to zero side force and a

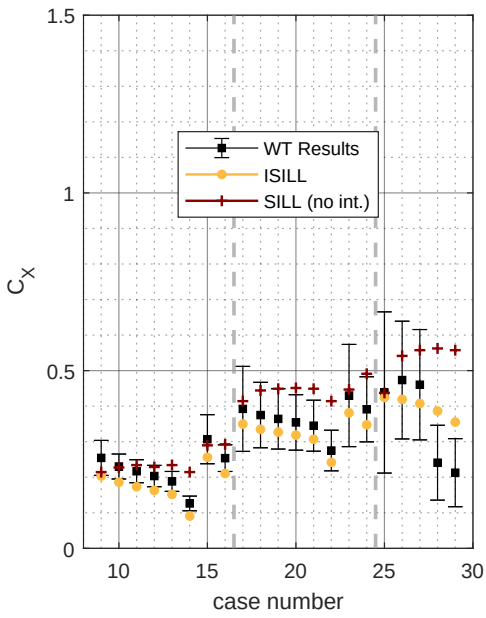

(a) Total driving force coefficient

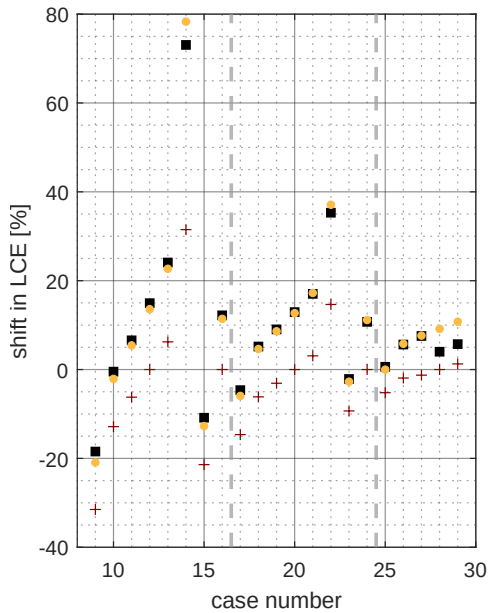

(b) Shift in longitudinal center of effort

Figure 5.4: Scatter plots of aggregated results for validation cases $T9$–$T29$ when the ship is sailing at $\beta_{AW} = 15°$.

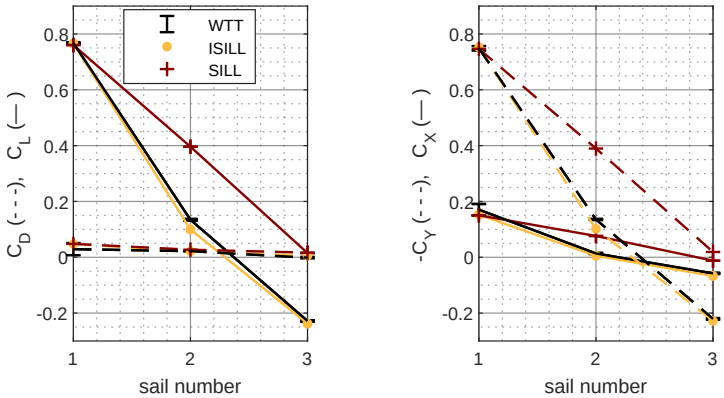

(a) Lift and drag force coefficients for each sail

(b) Driving and side force coefficients for each sail

Figure 5.5: Details for one validation case $T14$ at $\beta_{AW} = 15°$.

positive side force. It can be noted that even though Sail 3 is sheeted to $\alpha_3 = 0$, it generates a negative lift force and positive side force due to interaction effects. This behavior is captured well by the ISILL method.

Figure 5.6 presents scatter plots for the apparent wind angle of 30°. The driving force is doubled in most validation cases due to the ship's more favorable wind angle. As the angle of attack and the load increase, the ISILL method predicts a somewhat lower driving force than the wind tunnel tests. Studying the distribution of the driving force over the sails in the highlighted cases 20 and 26 in Figure 5.7(a) and Figure 5.7(b), the difference seems to be due to the ISILL method predicting a lower force generated by the upwind sail compared to the wind tunnel tests. In case $T26$, which is the validation case where the highest driving force is generated, the difference in total force is 8%.

Still, the ISILL method captures the general trends of the interaction effects well. The SILL model, not considering interaction, predicts a higher driving force than the wind tunnel tests for several cases. The most favorable type of sheeting is found for the first validation cases in each group, where Sail 1 is eased 3°–5° and Sail 3 is tightened with 3°–5° to compensate for the change in local angle of attack. The ISILL method correctly predicts the decrease of driving force in cases $T26$–$T29$, seen in Figure 5.6, but the case with the highest total driving force is predicted to be case $T25$ and not case $T26$. Studying case $T28$, detailed in Figure 5.7(c), it can be seen that according to the wind tunnel tests Sail 1 has stalled. The ISILL method did not predict this stall.

Consistent with the results for $\beta_{AW} = 15°$, the difference is small when comparing the shift in LCE for the ISILL method and the wind tunnel tests. The correspondence is largely improved by considering the interaction effects as SILL, without interaction, predicts a smaller shift than the wind tunnel tests.

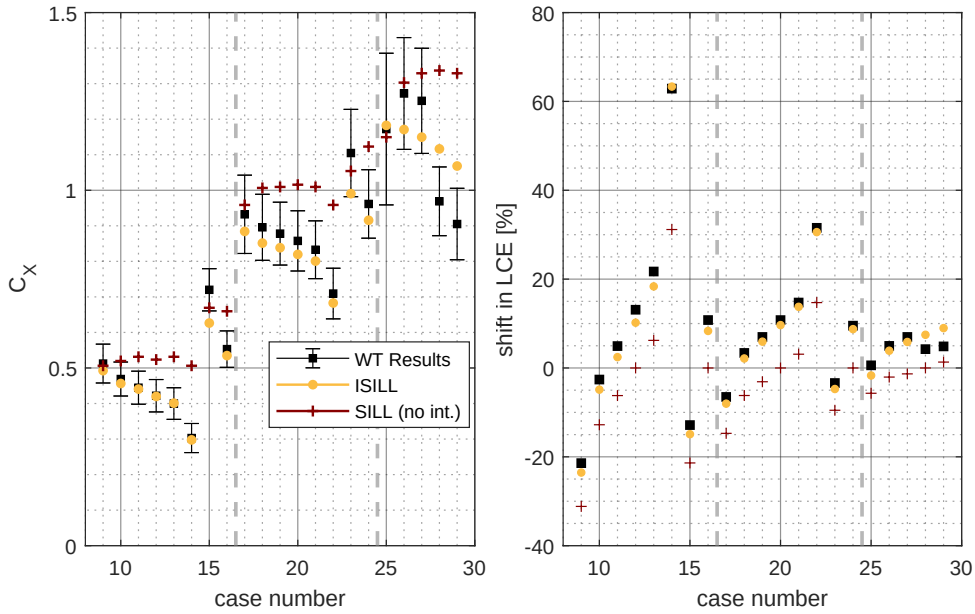

(a) Total driving force coefficient

(b) Shift in longitudinal center of effort

Figure 5.6: Scatter plots of aggregated results for validation cases $T9$–$T29$ when the ship is sailing at $\beta_{AW} = 30°$.

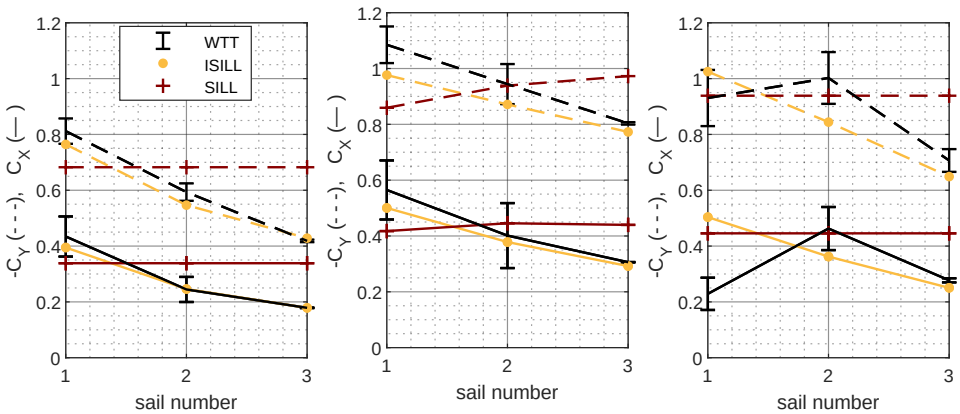

(a) Validation case $T20$ where the sails are equally sheeted to angles $\alpha_1 = \alpha_2 = \alpha_3 = 10°$.

(b) Validation case $T26$, where $\alpha_1 = 13°$, $\alpha_2 = 15°$ and $\alpha_3 = 17°$generates the highest driving force.

(c) Validation case $T28$ where $\alpha_1 = \alpha_2 = \alpha_3 = 15°$. Sail 1 has stalled in the wind tunnel tests.

Figure 5.7: Highlighted validation cases where the driving force coefficient and side force coefficient are plotted for each sail, sailing at $\beta_{AW} = 30°$.

5.4.1.2 Sailing at a close reach, $\beta_{AW} = 60°$

When the ship is sailing at a close reach, $\beta = 60°$, similar trends can be observed as for $\beta_{AW} = 30°$. However, the driving force has increased even further (observe the change in scale between Figure 5.6(a) and Figure 5.8(a)). When comparing ISILL to the wind tunnel tests, the difference for the validation case with the highest driving force, case $T27$ seen in Figure 5.9(b), is 12%. It is not only the forces on the upwind sail that the ISILL method underpredicts compared to the wind tunnel tests; in fact, the negative effect of the interaction seems to be well-balanced between the sails but equally overestimated by ISILL. The difference can be seen when comparing case $T20$ for the two different apparent wind angles $\beta_{AW} = 30°$ and $\beta_{AW} = 60°$ in Figure 5.7(a) and Figure 5.9(a).

Correspondence between ISILL and the wind tunnel tests is good when it comes to the shift in LCE, as seen in Figure 5.8(b). However, when the apparent wind angle increases, the sail's combined center of effort is less affected by interaction.

Returning to case $T28$ but now for $\beta = 60°$ (see Figure 5.9(c)) the stall prediction once again differs between the ISILL method and the experiments. The front sail has stalled quite drastically according to the experiments. However, the ISILL method, in contrast to SILL, does once again predict the same decrease in the total driving force seen in the wind tunnel tests for cases $T28$–$T29$. Capturing this decrease, and the maximum driving force, is important for sheeting optimization.

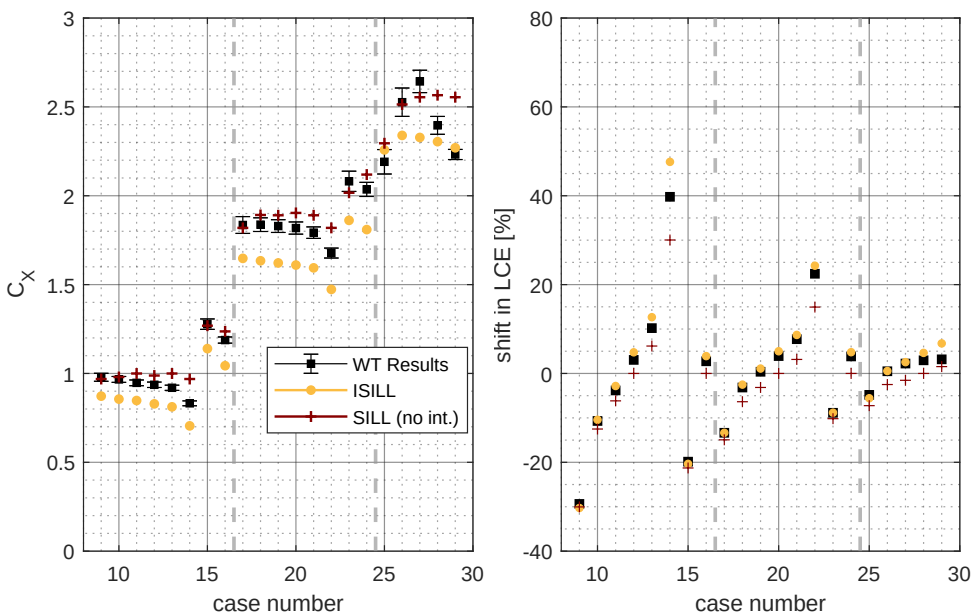

(a) Total driving force coefficient

(b) Shift in longitudinal center of effort

Figure 5.8: Scatter plots of aggregated results for validation cases $T9$–$T29$ when the ship is sailing at $\beta_{AW} = 60°$.

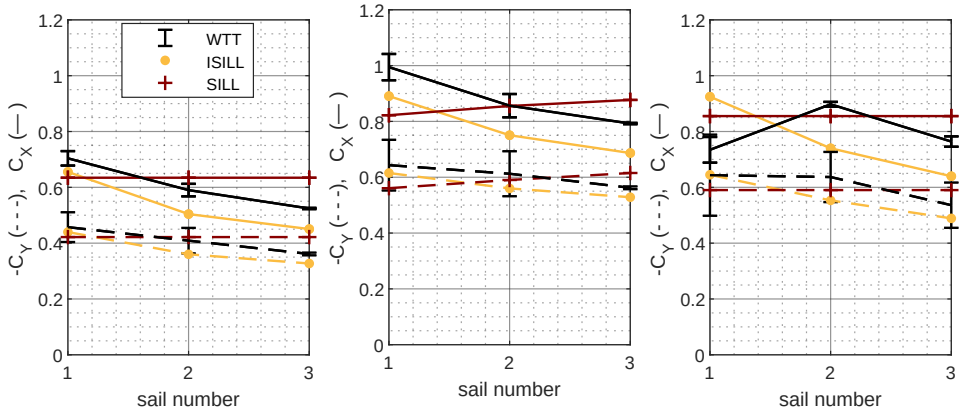

(a) Validation case $T20$ where the sails are equally sheeted to angles $\alpha_1 = \alpha_2 = \alpha_3 = 10°$.

(b) Validation case $T27$, where $\alpha_1 = 14°$, $\alpha_2 = 15°$ and $\alpha_3 = 16°$generates the highest driving force.

(c) Validation case $T28$ where $\alpha_1 = \alpha_2 = \alpha_3 = 15°$. Sail 1 has stalled in the wind tunnel tests.

Figure 5.9: Highlighted validation cases where the driving force coefficient and side force coefficient are plotted for each sail, sailing at $\beta_{AW} = 60°$.

5.4.1.3 Sailing at beam reach, $\beta_{AW} = 90°$

Validation results for when the ship is sailing at $\beta_{AW} = 90°$ are presented in Figure 5.10 and Figure 5.11. Sailing at beam reach generates the highest driving forces and the smallest shift in the sails' longitudinal center of effort. However, there is an effect of the interaction resulting in a decreased driving force compared to if the three sails would be unaffected by each other. The validation case predicted to have the highest driving force is the same for the ISILL method as for the experiments, but in general ISILL predicts a lower driving force.

For $\beta_{AW} = 90°$ the effect of interaction is relatively small. The difference in predicted shift in LCE is small between ISILL and SILL, and both versions generally correlate well with the wind tunnel tests in Figure 5.10(b). There is a quite large difference in the predicted shift in LCE for case $T25$ compared to the other validation cases. Case $T25$ is detailed in Figure 5.11(b), and it can be seen that Sail 3 has stalled in the wind tunnel tests, but it has not according to the ISILL method.

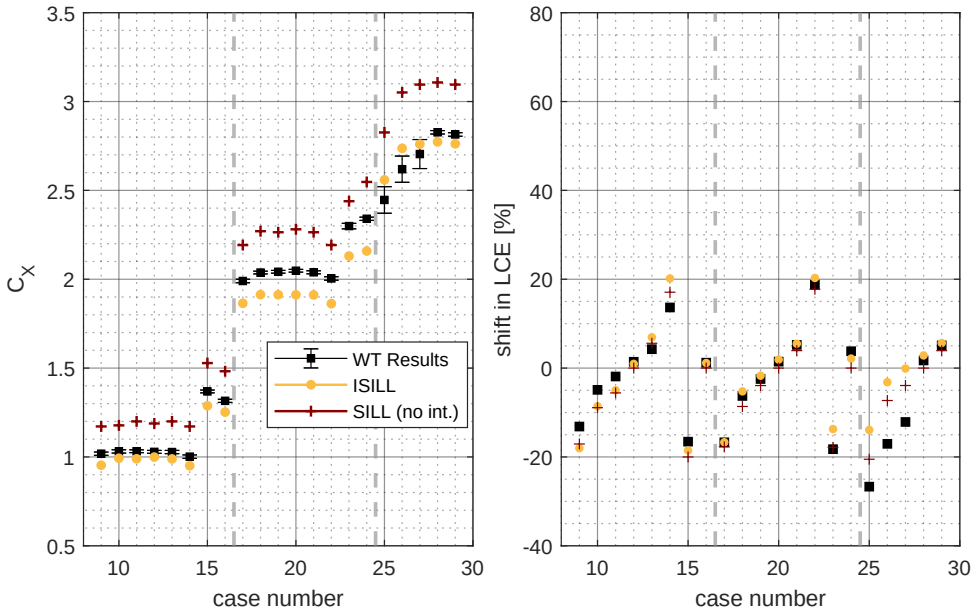

(a) Total driving force coefficient

(b) Shift in longitudinal center of effort

Figure 5.10: Scatter plots of aggregated results for validation cases $T9$–$T29$ when the ship is sailing at $\beta_{AW} = 90°$.

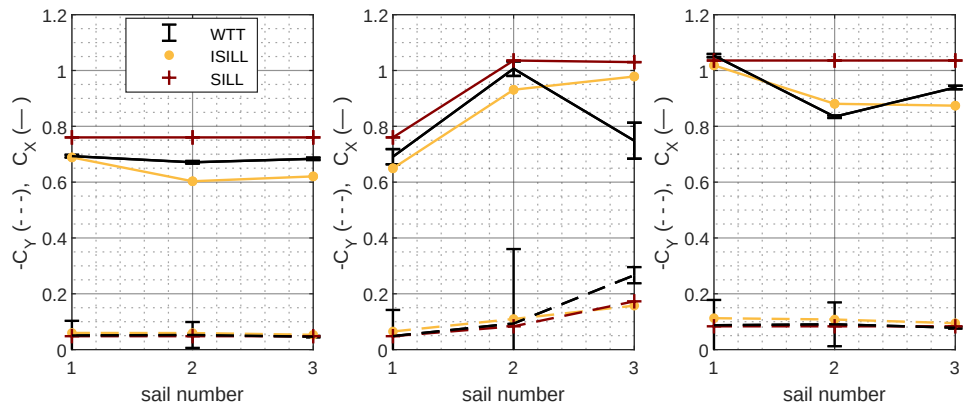

(a) Validation case $T20$ where the sails are equally sheeted to angles $\alpha_1 = \alpha_2 = \alpha_3 = 10°$.

(b) Validation case $T25$, where $\alpha_1 = 10°$, $\alpha_2 = 15°$ and $\alpha_3 = 20°$. Sail 3 has stalled.

(c) Validation case $T28$, where $\alpha_1 = \alpha_2 = \alpha_3 = 15°$, generates the highest driving force.

Figure 5.11: Highlighted validation cases where the driving and side force coefficient are plotted for each sail, sailing at $\beta_{AW} = 90°$.

5.4.2 Stall study - sheeting sweep with Sail 2

This section presents results for the sheeting sweep with Sail 2, corresponding to validation cases $S4$–$S16$. Only validation cases when sailing at $\beta_{AW} = 30°$ are available. Figure 5.12 gives the driving force and Figure 5.13 the side force for all three sails during the sweep. Even though only Sail 2 moves, an effect is seen also on the forces generated by Sail 1 and Sail 3. For example, the driving force generated by Sail 3 is almost halved compared to when not considering interaction (see SILL) when Sail 2 reaches $\alpha_2 = 20°$.

Consistent with previous results, the ISILL method captures the effect of the interaction well, but to some extent it predicts lower loads than in the experiments. The angle at which the maximum driving force and side force are generated are predicted accurately. Sweeping Sail 2, the change in local angle of attack for this sail due to interaction is relatively small only 2°. If instead Sail 1 or Sail 3 would had been swept, larger shifts in local angle of attack would have been seen, as was illustrated in the 2D sweeps with three profiles in Figure 4.4 and Figure 4.5. This is not because interaction effects are not present around Sail 2, but the effects of the upwind sail and the downwind sail are counteracting each other where the middle sail is placed.

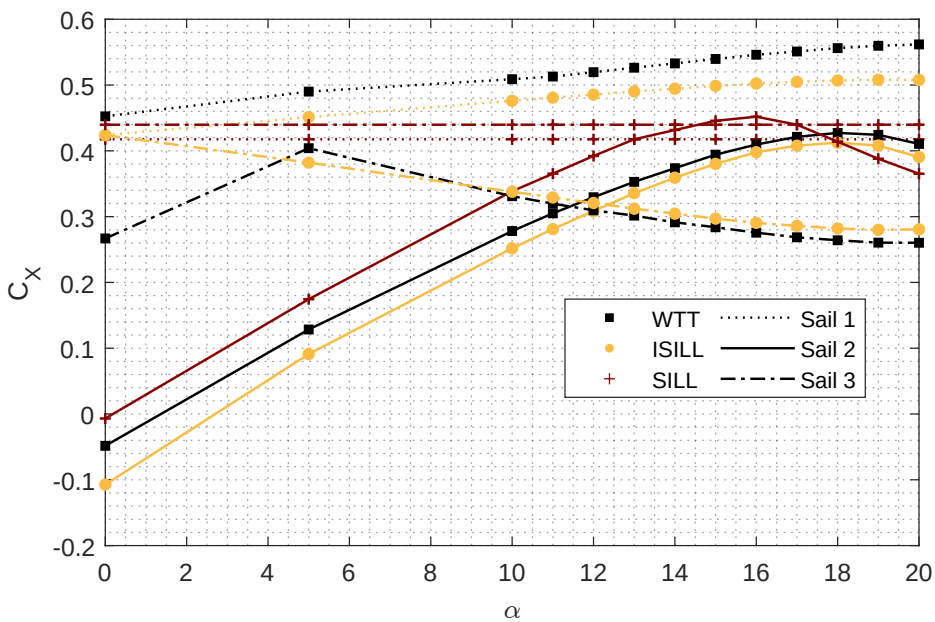

Figure 5.12: Driving force coefficient for Sail 1–Sail 3 when Sail 2 is swept from 0° to 20°, sailing at $\beta_{AW} = 30°$.

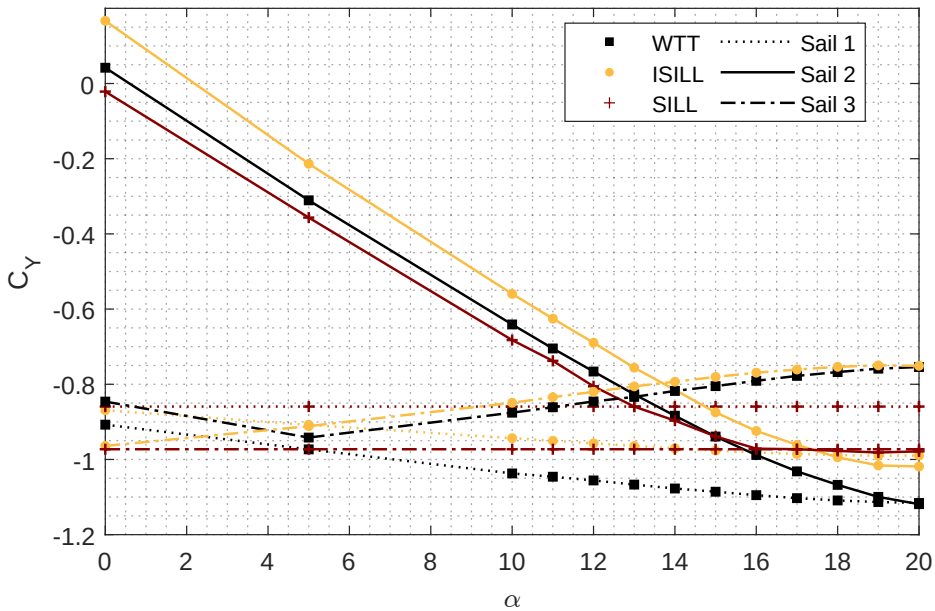

Figure 5.13: Side force coefficient for Sail 1–Sail 3 when Sail 2 is swept from 0° to 20°, sailing at $\beta_{AW} = 30°$.

Chapter 6

DISCUSSION

6.1 Validation Study I

In Validation Study I, two versions of the aerodynamic interaction method (ISILL and ISILL+BL) and the SILL code (no interaction considered) were compared to full-scale CFD simulations. The angle of attack sweep in 2D with three wingsail profiles showed that the total driving force was affected by the interaction and that it had a positive effect on the driving force in upwind conditions. However, the interaction negatively affected the driving force in beam reach conditions. Both ISILL and ISILL+BL considerably improved the prediction of the stall angle and the driving force compared to SILL, but ISILL underestimated the peak force in some cases. ISILL+BL predicted the stall angle for all three profiles within an accuracy of 2°, whereas SILL, not considering interaction, was off by 5° in the worst case. The largest prediction improvements were seen for the yaw moment coefficient, which is essential for predicting the maneuverability of the ship. In some upwind cases, an error in the yaw moment remained, up to 10%, yet the improvement compared to SILL was large, where the error was up to 70%.

In 3D, the codes were validated against 3D RANS CFD simulations for a few validation cases. Both versions of the proposed method predicted the effect that the interaction had on each sail well for all tested apparent wind angles. In the majority of the 3D validation cases, all the sails were sheeted to pre-stalling angles, and as expected there was little difference between the two versions, ISILL and ISILL+BL. There was one exception; in the last validation case where the foremost sail was close to stalling, ISILL+BL improved the prediction. No full stall study with sheeting sweeps was carried out in 3D due to computational limits.

Validation Study I showed that the interaction between the sails needs to be considered, especially for upwind sailing, and that extending the one-sail code SILL with a horseshoe vortex-based interaction model improved the prediction of forces and moments. Using a similar approach to model the interaction between two tandem airplane wings, Phillips and Snyder (2000) concluded that the LLT-based model could predict the inviscid forces with an accuracy as good as CFD. The ISILL method shows equal accuracy for pre-stall angles in Validation Study I.

The accuracy of the ISILL method was also consistent with the single-sail viscous lifting-line-based codes presented by Graf et al. (2014) and Persson et al. (2019), where the lift and drag forces were very well predicted for pre-stall angles. However, also in these studies, there were some discrepancies between the lifting-line codes and the RANS CFD simulations when comparing stall angles and maximum loads. Since the ISILL method inherits the accuracy of SILL, capturing the stalling point precisely in 3D cannot be expected. Yet, by having introduced viscous effects in the lifting-line codes, the stalling point and maximum lift seem to be estimated at an acceptable accuracy level. This is impossible with pure potential-flow calculations, for example

using the VLM-based code compared to the ISILL method in Paper II.

The boundary layer correction suggested in Validation Study I has a physical foundation, the influence of the adverse pressure gradient on separation. However, it requires CFD or other data for calibration, which may be impractical. yet, only a few 2D CFD cases are required to get a correction that is applicable for all sheeting angles. When implementing the method into, for example, a velocity prediction program (VPP), there is an option to use this correction or not from case to case, depending on the time available and the required accuracy. Without the correction, Validation Study I shows that ISILL is somewhat conservative in its power predictions.

The ISILL method is very quick compared to tools of higher fidelity, such as CFD or wind tunnel tests. The total computational cost, including the cost of generating 2D CFD input data and calibrating the boundary layer correction, is negligible compared to the cost of multiple 3D CFD simulations. The 3D validation cases run in a few seconds on a standard desktop computer with a code that has not been optimized for speed. The only input required is pre-tabulated 2D lift and drag data for the profile, which can be obtained using 2D CFD at a relatively low computational cost. In contrast, simulating one of the 3D validation cases using RANS CFD requires several hours of simulation time on a high-performance cluster (the calculations were performed on the Vera cluster, running on 30 nodes with 96 GB RAM). As highlighted already in Chapter 1, rapid tools that complement the more costly high-fidelity methods are crucial when designing and selecting a WPS for a certain application. Because the system's performance and fuel-saving potential are highly dependent on the ship's route and the weather, a large number of simulations for varying conditions is needed. The ISILL method is quick enough to run in real-time simulators and has been implemented in a commercial ship's simulator and VPP SEAMAN (Gerhardt et al., 2022).

6.2 Validation Study II

The aggregated results presented in Validation Study II demonstrated that the ISILL method improved the force prediction for interacting sails compared to not considering interaction. For the two lower apparent wind angles tested (15° and 30°), there was good correspondence between ISILL and the measurements, both regarding the total driving force and the shift in the sails' longitudinal center of effort. For the two higher apparent wind angles (60° and 90°), the total driving force predicted by ISILL was in general lower compared to the wind tunnel tests. The difference was up to 12% for some validation cases. Yet, the ISILL method was still able to predict the general behavior of the interaction, especially how the longitudinal center of effort of the sails was affected.

A few validation cases at higher angles of attack indicated that the foremost and aftmost sails sometimes stalled at a lower angle of attack and more drastically in the measurements than predicted by ISILL. However, the angle of attack sweep with the middle sail (at $\beta_{AW} = 30°$) showed good correspondence for the point of stall when comparing the measurements and ISILL. Both indicated the same angle of attack

generating the maximum driving force.

In Validation Study I, it was assumed that the CFD calculations were correct and that any disagreement between ISILL and CFD was caused by limitations in the ISILL method. Because the wind tunnel tests have not been corrected for blockage effects, the same conclusion cannot be drawn when validating against them. Blockage effects due to the tunnel walls lead to an increased wind speed and an increased local angle of attack for the sails, which would explain both the higher forces and earlier stall found in the wind tunnel measurements. The largest differences are seen for the high apparent wind angles, where the largest blockage effects would also be present because the sails come closer to the tunnel walls. Yet, the difference between ISILL and the measurements can have several explanations and can only be established after further post-processing of the wind tunnel data.

In the presentation of the single-sail calibration, it could be seen that the correspondence between SILL and the wind tunnel tests was very good for low angles of attack, and no calibration of the input table was needed here. This is consistent with a study by Barlas et al. (2021), where a lifting-line code was compared to wind tunnel tests for a single rotor blade for a wind turbine.

In Validation Study II, the 2D input data to the ISILL method was calibrated using 3D results for a single sail. This approach minimizes errors due to inaccurate 2D input data and limitations in the one-sail SILL model. 3D single-sail data may well be available at a reasonable cost, for example through wind tunnel testing or 3D CFD. In practice, tuning the input data using full-scale sea trials with single sails or rotors is also a possible approach, used for example by Werner et al. (2021). The tuned method can then be used in VPP to generate estimates of key performance indicators for the WPS en route over time.

6.3 Limitations and Recommendations

In this thesis, care has been taken to propose a method that can be generalized and applied to systems other than the test case used in this thesis. However, the test case evaluated here is limited when it comes to the type of sail, sail geometry, rig placement and evaluated apparent wind angles. Only a uniform inflow distribution has been tested. For example, the sails are of high aspect ratio and stand in a row, where the direct wake of an upwind sail cannot reach a downwind sail for any of the tested apparent wind angles.

From a theoretical viewpoint, the proposed interaction model should be a suitable approach for modeling the interaction between, for example, Flettner rotors, excluding areas in the viscous wake regions. Bordogna (2016) suggested a correction of the velocities in this region, which could be an appropriate addition to the ISILL method. However, modeling of wingsails with flaps, Flettner rotors or active sails may require introducing new input variables, such as flap angle, rotational speed and fan speed.

Another effect regarding the wake not considered in this thesis is the singularity point in the middle of the free wake vortex at which the induced velocities approach infinity. In a configuration where the free vortices in the wake directly reach other

sails, viscous damping of the vortex center should be applied. This approach has been successfully implemented in the ship simulation tool SHIPFLOW Motions (a time-accurate fully nonlinear boundary element method) where ISILL is used to model the sail forces (Kjellberg et al., 2022). In addition, a further improvement of the wake modeling would be to accept some unsteady modeling, where for example the location of the free vortices can adapt in each timestep.

It should be noted that the method presented in this thesis only considers sail–sail interaction. Another important effect to consider is the aerodynamic interaction between WPSs and a ship's superstructure and hull.

Regarding the prediction of the point of stall, it is likely that ISILL's prediction can be improved by combining the interaction model with an updated single-sail lifting-line model. For example, the SILL model used in this thesis applies an assumption of an elliptical lift distribution regardless of wing geometry and locally induced wind conditions. This assumption has the benefit of being very computationally stable and efficient. Still, there exist non-linear lifting-line methods that allow for a more correct representation of the lift distribution at a comparatively low added computational cost. This approach could prove necessary for other types of geometries than the wingsail tested in this thesis.

Chapter 7

CONCLUSIONS

This research aimed to formulate a rapid aerodynamic interaction method that considers sail–sail interaction effects that include key viscous effects, such as stall. The proposed method combines pre-calculated viscous 2D data with a 3D potential flow-based model. This makes it possible for the method to predict viscous effects while keeping the method very computationally efficient.

Based on two validation studies, comparing the method to CFD and wind tunnel tests, it can be concluded that the proposed interaction model improves the predicted forces and moments generated by the WPS considerably compared to not considering interaction. The improvement was especially large when studying the generated moments and the sails' combined longitudinal center of effort. This ability to predict a correct moment has important implications when it comes to sailing and ship design in practice because it determines the balance of the ship.

It was found that the method in general can predict the total driving force and total side force well. The correspondence with the validation data was very good for low angles of attack, except for some wind tunnel validation cases where blockage effects are a likely explanation for the deviations. When nearing stalling angles, the difference between the method's prediction and the validation data increases. In some cases, the ISILL method underpredicts the maximum driving force by approximately 5%–7% compared to CFD simulations. Ideally, the accuracy of the ISILL method close to stalling angles should be high to properly capture the correct maximal total driving force and moments. Even with further improvements in the method, it is likely that complementary simulations with high-fidelity tools will be needed at some stages in a ship design process. Yet, the results indicate that the proposed rapid method is accurate enough to be a suitable tool for estimating the total driving force of the WPS, the sails' combined longitudinal center of effort and the sails' optimal sheeting angles. The ability to do so at a low computational (and financial) cost is important in early ship design, optimization and VPPs.

To better capture the effect of postponed stall on upwind sails due to the sail–sail interaction, a boundary layer correction to the original method was suggested. Where it was tested, the results indicated good potential to further increase accuracy using the correction. However, the correction comes with an added cost because it requires additional preparatory simulations for calibration.

Chapter 8

FUTURE WORK

Following are suggestions for future work:

- Further development of the ISILL method
- Further validation of the ISILL method
- Extending the wind tunnel test validation study
- Implementation of the ISILL method in the WPS and ship design process

Several limitations of the method were discussed in Section 6.3, where a few further developments to improve accuracy and increase the range of application of the method were suggested. This includes refining the modeling of the wake system, considering, for example, viscous and in-stationary effects. In addition, the single-sail model SILL used together with the sail–sail interaction model is based on several simplifications. One example is the assumption of an elliptical lift distribution. The lift distribution could instead be updated in an iterative process based on the sail's actual geometry and the surrounding flow. An iterative process coupled with the interaction model could also improve the method's predictions close to stall. Another area of development is to establish a suitable correction for hull–sail interaction effects.

In developing the aerodynamic method, care has been taken to ensure its applicability to general WPSs and not only to rigid wingsails. Yet, it remains to validate the ISILL method for other types of WPSs and in different geometrical configurations. For example, new systems to test are wingsails with flaps, Flettner rotors and different types of active sails, as they are also present on the WPS market. In order to establish the method's accuracy for different design alternatives, studies with different sail-to-sail spacing and rig placements are needed. Other variables to consider in further validation studies are varying wind conditions and atmospheric boundary layer profiles. Some validation studies of the types mentioned above have already been performed outside of the work within this thesis, but they need to be structured and documented. Finally, further investigations regarding the ISILL method's accuracy close to the point of stall are of high interest, as it is crucial for predicting the maximal forward propulsive force generated by the WPS.

To be able to draw further conclusions from the validation against wind tunnel tests (Validation Study II) presented in this thesis, the blockage effects in the tunnel need to be established and the wind tunnel data corrected for these. This can be done either by CFD simulation or by potential-flow codes where the tunnel walls are mirrored. There is also additional data available for further analysis of the sail–sail interaction effects, such as particle image velocimetry (PIV) measurements of the wake behind the sails and pressure tap measurements along the sail span.

When designing a ship equipped with wind-assisted propulsion, and especially ships where wind power is expected to contribute to a major part of the propulsion,

the WPS design needs to be an integrated part of the overall design process. To evaluate the performance of a WPS, several tools with different fidelity levels are available. These tools come with different computational and financial costs. How are the tools best combined to efficiently evaluate and optimize ship designs? Rapid low-fidelity tools can be applied in the early stages of ship design where many different design concepts might be evaluated in parallel, but also in the final stages since rapid tools are needed to evaluate performance en route due to the many varying wind conditions a ship may experience. Still, applying high-fidelity tools such as 3D CFD or model testing of the whole ship is likely to be necessary to confirm, for example, the ship's final maneuverability. Combining the different tools efficiently to make trustworthy performance predictions is an important enabler for getting more WPSs from the drawing table to the ocean.

References

Abbot, I. H. and Doenhoff, A. E. von (1959). *Theory of wing sections*. 2nd edition. New York: Dover Publications, Inc.

Anderson, J. D. (2017). *Fundamentals of aerodynamics*. 6th edition. New York: McGraw-Hill. ISBN: 978-1-259-12991-9.

Barlas, T., Pirrung, G. R., Ramos-García, N., Horcas, S. G., Mikkelsen, R. F., Olsen, A. S., and Gaunaa, M. (2021). "Wind tunnel testing of a swept tip shape and comparison with multi-fidelity aerodynamic simulations". In: *Wind Energy Science* 6.5, pp. 1311–1324. ISSN: 23667451. DOI: 10.5194/wes-6-1311-2021.

Barlow, J. B., Rae, W. H. J., and Pope, A. (1999). *Low-Speed Wind Tunnel testing*. 3rd edition. New York: John Wiley & Sons. ISBN: 0471557749.

Bertagnolio, F. (2008). *NACA0015 measurements in LM wind tunnel and turbulence generated noise*. Tech. rep. Risoe-R No. 1657 (EN). Danmarks Tekniske Universitet, Risø Nationallaboratoriet for Bæredygtig Energi.

Bordogna, G. (2016). "Validation of a simple aerodynamic model capable to predict the interaction effects occuring between two generic wind propulsion systems". In: *The 12th International Conference on Hydrodynamics*. September 18–23, Egmond aan Zee, The Netherlands.

Bordogna, G., Keuning, J. A., Huijsmans, R. H., and Belloli, M. (2018). "Wind-tunnel experiments on the aerodynamic interaction between two rigid sails used for wind-assisted propulsion". In: *International Shipbuilding Progress* 65.1, pp. 93–125. ISSN: 15662829. DOI: 10.3233/ISP-180143.

Bordogna, G. (2020). "Aerodynamics of wind-assisted ships Interaction effects on the aerodynamic performance of multiple wind-propulsion systems". PhD thesis. ISBN: 9789055841745. DOI: 10.4233/uuid:96eda9cd-3163-4c6b-9b9f-e9fa329df071.

Cairns, J., Vezza, M., Green, R., and MacVicar, D. (2021). "Numerical optimisation of a ship wind-assisted propulsion system using blowing and suction over a range of wind conditions". In: *Ocean Engineering* 240, p. 109903. ISSN: 00298018. DOI: 10.1016/J.OCEANENG.2021.109903.

Castro, I. P. (2001). *Calibration tests in the working section of the R J Mitchell Wind Tunnel*. Tech. rep. University of Southampton.

Chapin, V. G., Neyhousser, R., Dulliand, G., and Chassaing, P. (2006). "Analysis, design and optimization of Navier-Stokes flows around interacting sails". In: *MDY06 International Symposium on Yacht Design and Production*. March 30–31, Madrid, Spain.

Cheng, H. and Wang, H. (2018). "Prediction of Lift Coefficient for Tandem Wing Configuration or Multiple-Lifting-Surface System Using Prandtl's Lifting-Line Theory". In: *Journal of Aerospace Engineering* Volume 2018. DOI: 10.1155/2018/3104902.

Chou, T., Kosmas, V., Renken, K., and Acciaro, M. (2020). *New Wind Propulsion Technology - A Literature Review of Recent Adoptions*. Report D 5.B. Interreg North Sea Europe Wind Assisted Ship Propulsion (WASP). https://northsearegion.eu/wasp/output-library-publications/.

DNV (2021). *Energy Transition Outlook 2021, Maritime Forecast to 2050*. Det Norske Veritas Group. www.dnv.com/maritime/publications/maritime-forecast-2022/index.html.

Eça, L. and Hoekstra, M. (2014). "A procedure for the estimation of the numerical uncertainty of CFD calculations based on grid refinement studies". In: *Journal of Computational Physics* 262, pp. 104–130. ISSN: 10902716. DOI: 10.1016/j.jcp.2014.01.006.

Eça, L., Vaz, G., Toxopeus, S. L., and Hoekstra, M. (2019). "Numerical errors in unsteady flow simulations". In: *Journal of Verification, Validation and Uncertainty Quantification* 4.2, pp. 1–10. ISSN: 23772166. DOI: 10.1115/1.4043975.

Fujiwara, T., Hearn, G. E., Kitamura, F., and Ueno, M. (2005). "Sail-sail and sail-hull interaction effects of hybrid-sail assisted bulk carrier". In: *Journal of Marine Science and Technology* 10.2, pp. 82–95. ISSN: 09484280. DOI: 10.1007/s00773-005-0191-4.

Gerhardt, F. C., Werner, S., Li, D.-q., and Malmek, K. (2022). "Levelling the playing field: A numerical platform for the fair comparison of wind propulsion systems". In: *International Conference on High Performance Marine Vehicles*. August 29–31, Cortona, Italy.

Graf, K., Hoeve, A. V., and Watin, S. (2014). "Comparison of full 3D-RANS simulations with 2D-RANS/lifting line method calculations for the flow analysis of rigid wings for high performance multihulls". In: *Ocean Engineering* 90, pp. 49–61. ISSN: 00298018. DOI: 10.1016/j.oceaneng.2014.06.044.

Ingham, P. and Tersløv, O. (1985). "Wind tunnel tests and manoeuvre simulator tests with different types of sails and ships". In: *Journal of Wind Engineering and Industrial Aerodynamics* 20.1-3, pp. 169–185. ISSN: 01676105. DOI: 10.1016/0167-6105(85)90017-0.

Katz, J. and Plotkin, A. (2001). *Low-Speed Aerodynamics*. Cambridge: Cambridge University Press. ISBN: 978-0-521-66219-2.

Kjellberg, M., Gerhardt, F., and Werner, S. (2022). "Sailing in waves: A numerical method for analysis of seakeeping performance and dynamic behavior of a wind powered ship". In: *SNAME 24th Chesapeake Sailing Yacht Symposium*. June 10–11, Annapolis, Maryland. DOI: 10.5957/CSYS-2022-013.

Lee, H., Jo, Y., Lee, D. J., and Choi, S. (2016). "Surrogate model based design optimization of multiple wing sails considering flow interaction effect". In: *Ocean Engineering* 121, pp. 422–436. ISSN: 00298018. DOI: 10.1016/j.oceaneng.2016.05.051.

Li, Q., Nihei, Y., Nakashima, T., and Ikeda, Y. (2015). "A study on the performance of cascade hard sails and sail-equipped vessels". In: *Ocean Engineering* 98, pp. 23–31. ISSN: 00298018. DOI: 10.1016/j.oceaneng.2015.02.005.

Lu, R. and Ringsberg, J. W. (2020). "Ship energy performance study of three wind-assisted ship propulsion technologies including a parametric study of the Flettner rotor technology". In: *Ships and Offshore Structures* 15.3, pp. 249–258. ISSN: 17445302. DOI: 10.1080/17445302.2019.1612544.

Malmek, K., Dhome, U., Larsson, L., Werner, S., Ringsberg, J., and Finnsgård, C. (2020). "Comparison of two rapid numerical methods for predicting the performance of multiple rigid wind-sails". In: *5th International Conference on Innovation in High Performance Sailing Yachts and Sail-Assisted Ship Propulsion*. June 15–17, Gothenburg, Sweden, pp. 49–58.

Marimon Giovannetti, L., Dhomé, U., Malmek, K., Persson, A., and Wielgosz, C. (2022). "Multi-wing sails interaction effects". In: *SNAME 24th Chesapeak Sailing Yatch Synopsium*. June 10–11, Annapolis, Maryland.

Nakashima, T., Yamashita, Y., Nihei, Y., and Li, Q. (2011). "A basic study for propulsive performance prediction of a cascade of wing sails considering their aerodynamic interaction". In: *International Offshore and Polar Engineering Conference*. Vol. 8. June 19–24, Maui, Hawaii, pp. 995–1001. ISBN: 9781880653968.

Ouchi, K., Uzawa, K., and Kanai, A. (2011). "Huge Hard Wing Sails for the Propulsor of Next Generation Sailing Vessel". In: *Second International Symposium on Marine Propulsors*. June 15–17, Hamburg, Germany.

Persson, A., Li, D.-Q., Olsson, F., Werner, S., and Dhomé, U. (2019). "Performance Prediction of Wind Propulsion Systems Using 3D CFD And Route Simulation". In: *RINA Wind Propulsion 2019*. October 15–16, London, UK, pp. 19–30.

Phillips, W. F. and Snyder, D. O. (2000). "Modern adaptation of Prandtl's classic lifting-line theory". In: *Journal of Aircraft* 37.4, pp. 662–670. ISSN: 00218669. DOI: 10.2514/2.2649.

Sheldahl, R. E. and Klimas, P. C. (1981). *Aerodynamic characteristics of seven symmetrical airfoil sections through 180-degree angle of attack for use in aerodynamic analysis of vertical axis wind turbines.* Tech. rep. SAND-80-2114. https://www.osti.gov/biblio/6548367. Albuquerque, NM United States: Sandia National Laboratories.

Siemens (2022). *Simcenter STAR-CCM+ 2022.1*. Build 17.02.007. Siemens Digital Industries Software. www.plm.automation.siemens.com/global/en/products/simcenter/STAR-CCM.html.

Spall, R. E., Phillips, W. F., and Pincock, B. B. (2013). "Numerical analysis of multiple, thin-sail geometries based on Prandtl's lifting-line theory". In: *Computers and Fluids* 82, pp. 29–37. ISSN: 00457930. DOI: 10.1016/j.compfluid.2013.04.020.

Tillig, F. (2020). "Simulation model of a ship's energy performance and transportation costs". PhD thesis. Chalmers University of Technology. ISBN: 9789179052836. https://research.chalmers.se/publication/516908.

Tillig, F. and Ringsberg, J. W. (2020). "Design, operation and analysis of wind-assisted cargo ships". In: *Ocean Engineering* 211. ISSN: 0029-8018. DOI: doi.org/10.1016/j.oceaneng.2020.107603.

Weissinger, J. (1947). *The lift distribution of swept-back wings*. Tech. rep. NACA-TM-1120. https://ntrs.nasa.gov/citations/20030064148. Zentrale fuer Wissenschaftliches Berichtswesen der Luftfahrtforschung des Generalluftzeugmeisters.

Werner, S., Nisbet, J., Hörteborn, A., and Nielsen, R. (2021). "Speed Trial Verification for a Wind Assisted Ship". In: *RINA Wind Propulsion 2021*. September 15-16, London, UK, pp. 15–16. DOI: 10.3940/rina.win.2021.09.